Space Sci Rev (2009) 145: 337–380
DOI 10.1007/s11214-009-9562-1

Solar Surface Magnetism and Irradiance on Time Scales from Days to the 11-Year Cycle

V. Domingo · I. Ermolli · P. Fox · C. Fröhlich · M. Haberreiter · N. Krivova · G. Kopp · W. Schmutz · S.K. Solanki · H.C. Spruit · Y. Unruh · A. Vögler

Received: 30 August 2007 / Accepted: 1 June 2009 / Published online: 24 July 2009

Abstract The uninterrupted measurement of the total solar irradiance during the last three solar cycles and an increasing amount of solar spectral irradiance measurements as well

V. Domingo (✉)
Grupo de Astronomía y Ciencias del Espacio, Laboratorio de Procesado de Imágenes, Universidad de Valencia, 46980 Paterna (Valencia), Spain
e-mail: vdomingo@uv.es

I. Ermolli
INAF Osservatorio Astronomico di Roma, 00040 Monte Porzio Catone, Italy
e-mail: ermolli@mporzio.astro.it

P. Fox
HAO/NCAR, Boulder, CO 80307-3000, USA
e-mail: pfox@ucar.edu

C. Fröhlich · W. Schmutz
Physikalisch-Meteorologisches Observatorium Davos, World Radiation Center, 7260 Davos Dorf, Switzerland

C. Fröhlich
e-mail: cfrohlich@pmodwrc.ch

W. Schmutz
e-mail: werner.schmutz@pmodwrc.ch

M. Haberreiter · G. Kopp
Laboratory for Atmospheric and Space Physics, University of Colorado, Boulder, CO 80303, USA

M. Haberreiter
e-mail: Margit.Haberreiter@lasp.colorado.edu

G. Kopp
e-mail: Greg.Kopp@LASP.Colorado.edu

N. Krivova · S.K. Solanki
Max-Planck-Institut für Sonnensystemforschung, 37191 Katlenburg-Lindau, Germany

N. Krivova
e-mail: natalie@mps.mpg.de

as solar imaging observations (magnetograms and photometric data) have stimulated the development of models attributing irradiance variations to solar surface magnetism. Here we review the current status of solar irradiance measurements and modelling efforts based on solar photospheric magnetic fields. Thereby we restrict ourselves to the study of solar variations from days to the solar cycle. Phenomenological models of the solar atmosphere in combination with imaging observations of solar electromagnetic radiation and measurements of the photospheric magnetic field have reached high enough quality to show that a large fraction (at least, about 80%) of the solar irradiance variability can be explained by the radiative effects of the magnetic activity present in the photosphere. Also, significant progress has been made with magnetohydrodynamic simulations of convection that allow us to relate the radiance of the photospheric magnetic structures to the observations.

Keywords Solar physics · Solar irradiance · Solar atmosphere · Solar variations · Solar magnetism · Irradiance variations · Solar activity

1 Introduction

Since the advent of magnetic field measurements on the Sun, it is known that solar activity is linked to the presence of magnetic flux in the solar photosphere. There is a large range of magnetic field structures in spatial size, flux intensity and topology evolving in time on different time scales. From quiet Sun internetwork to active regions, the magnetic field elements, generally constituted of bundles or groups of field lines (i.e. magnetic flux tubes), are found in sizes that reach from about 100 km to a significant fraction of the solar surface (Meunier 2003). Magnetic field strengths up to 6 kG (in an extreme case) are found in the photosphere, see Solanki (2003), Livingston et al. (2006) for distribution of sunspot magnetic fields, and Abramenko and Longcope (2005) for active region magnetic fields. The distribution in space and in time appears to be associated with the changing structure of the photospheric granulation and supergranulation, directly related to solar convection. The relative number of structures of different size and characteristics changes with a period of approximately 11 years, that coincides with the observed period of other solar activity indices. A general review on the present knowledge of the solar magnetic field can be found in Solanki et al. (2006).

One of the manifestations of solar activity is the variation of the solar irradiance, which is the total solar energy flux at 1 AU from the Sun. Brightening on the Sun at diverse

S.K. Solanki
School of Space Research, Kyung Hee University, Yongin, Gyeonggi 446-701, Korea
e-mail: solanki@mps.mpg.de

H.C. Spruit
Max-Planck-Institut für Astrophysik, 85741 Garching, Germany
e-mail: henk@mpa-garching.mpg.de

Y. Unruh
Astrophysics Group, Blackett Laboratory, Imperial College of Science, Technology and Medicine, London, SW7 2AZ, UK
e-mail: y.unruh@imperial.ac.uk

A. Vögler
Astronomical Institute Utrecht, 3584CC Utrecht, The Netherlands
e-mail: A.Voegler@astro.uu.nl

wavelengths as well as the presence of sunspots has been observed with ground based telescopes since long ago. Over the 30 years of the space-based irradiance measurements (Fröhlich 2006), the relationship between magnetic structures and associated brightness effects has been broadly studied by many groups (e.g., Willson et al. 1981; Hudson et al. 1982; Chapman 1984; Willson and Hudson 1988; Chapman et al. 1996; Fligge et al. 1998; Ermolli et al. 2003; Krivova et al. 2003; Wenzler et al. 2006, among others).

In the following we summarise the present understanding of the relationship between photospheric magnetism and irradiance changes. We restrict ourselves to the study of solar variations for the time when instrumental data are available. We also do not consider time scales shorter than a day, where the surface magnetic field is no longer the dominant driver of the variations (see e.g. Hudson 1988; Solanki et al. 2003; Woods et al. 2006).

In Sect. 2 we review the status of solar irradiance measurements, for total solar irradiance (TSI) in Sect. 2.1, and for spectral irradiance (SSI) in Sect. 2.2. Section 3 describes how solar photospheric magnetic fields affect the irradiance (Sect. 3.1) and how radiative MHD simulations of photospheric magnetoconvection are employed to connect the physical mechanism that underlies photospheric variations with irradiance changes (Sect. 3.2). Section 4 summarises the semi-empirical model atmospheres that have evolved in the recent years as part of irradiance calculations. Finally, Sect. 5 describes empirical reconstructions of solar irradiance from solar activity indices (Sect. 5.1) as well as semi-empirical models based on intensity images (Sect. 5.2) and magnetograms (Sect. 5.3).

2 Observation of Solar Irradiance

Here we describe the available observations of total and spectral solar irradiance (TSI and SSI). Solar irradiance is the Sun's energy flux received at a mean distance of 1 AU. We call it total when is integrated over all wavelengths.

2.1 Total Solar Irradiance

Since late 1978 total solar irradiance (TSI) measurements were made by different radiometers in space: Hickey-Frieden radiometer (HF) on the NOAA/NASA NIMBUS 7 mission (Hoyt et al. 1992), Active Cavity Radiometer for Irradiance Monitoring (ACRIM I) on the NASA Solar Maximum Mission (SMM) (Hudson and Willson 1981), ACRIM II on the NASA Upper Atmospheric Research Satellite (UARS) mission (Willson 1994), Variability of Irradiance and Gravity Oscillations (VIRGO) on the ESA/NASA mission Solar and Heliospheric Observatory (SoHO) (Fröhlich et al. 1997), ACRIM III on the NASA mission ACRIMSat (Willson 2001), and the Total Solar Irradiance Monitor (TIM) on the Solar Radiation and Climate Experiment (SoRCE) mission (Kopp and Lawrence 2005). These radiometers have a cavity to absorb solar radiation and a heat-flux transducer which is electrically-calibrated, hence the name Electrically Calibrated Radiometer (ECR, for details see Fröhlich 2009a, and references therein).

Figure 1a shows these original time series and it is clear that not only the absolute values are quite different, especially at the beginning of the series, but there are also other important differences between the series. Of the instruments, only the ACRIM, VIRGO, and TIM instruments have the ability to monitor in-flight degradation due to solar exposure; the benefit of this correction is obvious from comparison of early ACRIM-I with HF.

The individual time series—either as they are or corrected for some effects not considered in the original data sets—can be used for the construction of a TSI composite by

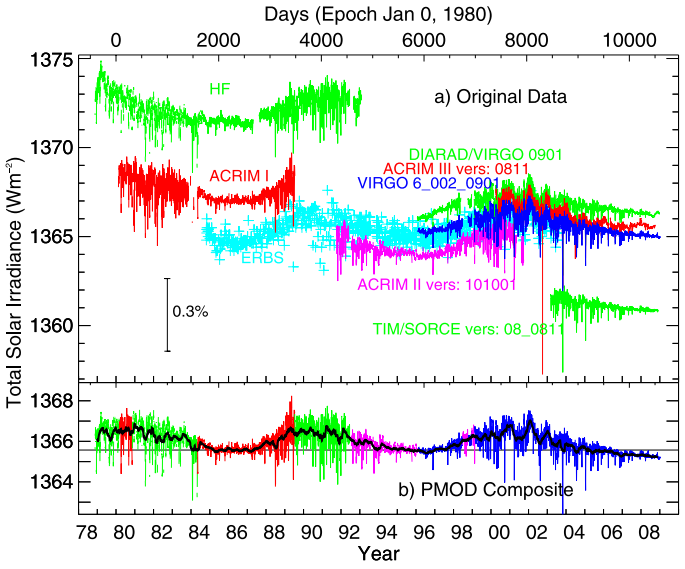

Fig. 1 (**a**) Daily averaged values of the Sun's total irradiance from radiometers on different space platforms as published by the instrument teams since November 1978. Note, that the VIRGO TSI is determined from both VIRGO radiometers (PMO6V and DIARAD), whereas the DIARAD TSI is from IRMB. Also plotted are data from ERBS (Lee III et al. 1987). Panel (**b**) shows the PMOD composite

shifting each series to a common level and merging them together. Presently there are three composites available, the first one was presented in 1997 at the IAU General Assembly in Kyoto by Fröhlich and Lean (1998b) and is now called the PMOD composite (originating form Physikalisch-Meteorologisches Observatorium Davos). A few months later the ACRIM composite (originating from the ACRIM team) was published by Willson (1997) and was updated in 2003 (Willson and Mordvinov 2003). Recently a third composite, called IRMB (originating from Institut Royale Météorlogique de Belgique), was presented by Dewitte et al. (2004). Although the three composites are based on the same original data sets major differences are found before 1981 and during the gap between the end of ACRIM-I and the beginning of ACRIM-II (so-called ACRIM gap from June 1989 until October 1991). Since the first publication of the ACRIM composite by Willson (1997) the main issue is whether a change of the radiometer HF on NIMBUS 7 has happened during the ACRIM-gap period as first suggested by Lee III et al. (1995), Chapman et al. (1996). Such a change is still neglected by the ACRIM team and thus their TSI shows a substantial increase of more than 0.5 W m^{-2} during cycle 22. A detailed re-analysis of the HF long-term behaviour by Fröhlich (2000, 2006) and comparison with ERBE data and the Kitt-Peak reconstruction (Wenzler et al. 2006) confirm the need for a correction of HF. The results of a similar reconstruction by Krivova et al. (2007) have now been used to 'resolve' this issue by Scafetta and Willson (2009). In contrast to the Kitt-Peak reconstruction the Krivova et al. (2007) one does not reproduce the details of the intra-cycle variability properly, because it is focused on the long-term variations back to the 17th century. Thus, these new arguments are only misleading and do not support the increase of TSI during cycle 22. We use here the PMOD composite, mainly because it has also a reliable cycle 21 and because it agrees best with the independent TSI record from ERBS (e.g. Fröhlich and Lean 2004) and the reconstruction from Kitt-Peak magnetograms (Wenzler et al. 2006, see also Fig. 13).

The most obvious feature of TSI variability is the modulation by the 11-year activity cycle of somewhat less than 0.1%. We define here the amplitude as if it would vary like a sine squared: the mean value over the period between two minima is multiplied by two and corrected for a linear trend during that cycle (by half of the difference between the minima). The values of the amplitudes are 0.9359, 0.8602, 0.9026 $\mathrm{W\,m^{-2}}$ for the cycles 21, 22 and 23, respectively. There are dips due to sunspots and brightening due to faculae, as first pointed out by Willson et al. (1981). The greatest dip of about $-4\ \mathrm{W\,m^{-2}}$ in this whole period was observed during the passage of large sunspot groups on October 31, 2003. The minima show a decrease from 1365.57 in 1986 over 1365.45 in 1996 down to 1365.23 $\mathrm{W\,m^{-2}}$ in 2009. This may indicate a long-term trend which will however not be discussed in this paper (see Sect. 1). The TSI amplitude of cycle 23 is higher than the earlier ones whereas the amplitudes of the other parameters such as e.g. the sunspot number show a constant decrease over the same period. This is explained by the fact that during cycle 23 there are extended periods when TSI is high due to large faculae in active regions without sunspots, which was not the case during cycles 21 and 22.

The PMOD, ACRIM and IRMB composites are available from http://www.pmodwrc.ch/pmod.php?topic=tsi/composite/SolarConstant, http://www.acrim.com/RESULTS/Composite/composite_acrim_hdr_1108.txt and http://remotesensing.oma.be/TSI/SARR.diarad.

2.2 Spectral Solar Irradiance

The TSI is the spectrally integrated solar radiation at 1 AU and is an essential component of the Earth's radiation budget. The absorption, scattering, or reflection of this energy by the Earth's atmosphere, clouds, or surface depend greatly on wavelength: the visible and near infrared (NIR) radiation not scattered by clouds largely affects the Earth's surface and troposphere, while the UV is absorbed in the troposphere and stratosphere. Similarly, the regions of the Sun's atmosphere from which this radiation originates are wavelength dependent, with the X-rays and ultraviolet coming mostly from the solar corona and transition region while the visible and IR emanate from the photosphere and chromosphere. While the TSI varies roughly by 0.1% over the solar cycle, energy at ultraviolet wavelengths can vary by over 100%, with X-ray variations being factors of over a hundred; so while most of the solar radiative energy is in the visible and NIR, the relative solar variability is greater in the UV (see Fig. 2). Thus an understanding of the solar processes responsible for emitted radiation as well as their effects on Earth's atmospheric and climate responses are greatly enhanced by knowledge of the solar spectral irradiance (SSI).

Measurements of SSI have been intermittent both temporally and spectrally, since they are driven by both Earth atmospheric and solar studies, each with preferred wavelength regions and resolutions. We summarise here space-borne SSI measurements in approximate order of increasing wavelength, and provide Internet links to each dataset.

The National Oceanic and Atmospheric Administration (NOAA) has flown X-Ray Sensors (XRS's) on their Geostationary Operational Environmental Satellites (GOES) since 1974 (Donnelly and Cowley 1977), providing the longest continual measurements of SSI in existence. These instruments are intended as monitors of solar eruptive events, so that they have a 3-sec cadence of reported measurements and nearly real-time telemetry. Two filter bandpasses on each XRS gas cell monitor the SSI in the 0.05 to 0.4 nm and 0.1 to 0.8 nm spectral regions, sampling high-energy solar events with an absolute accuracy of approximately 30%. Magnitudes of XRS flare signals determine solar flare classifications. Averaged X-ray Space Environment Monitor data are available from NOAA at http://goes.ngdc.noaa.gov/data/avg/.

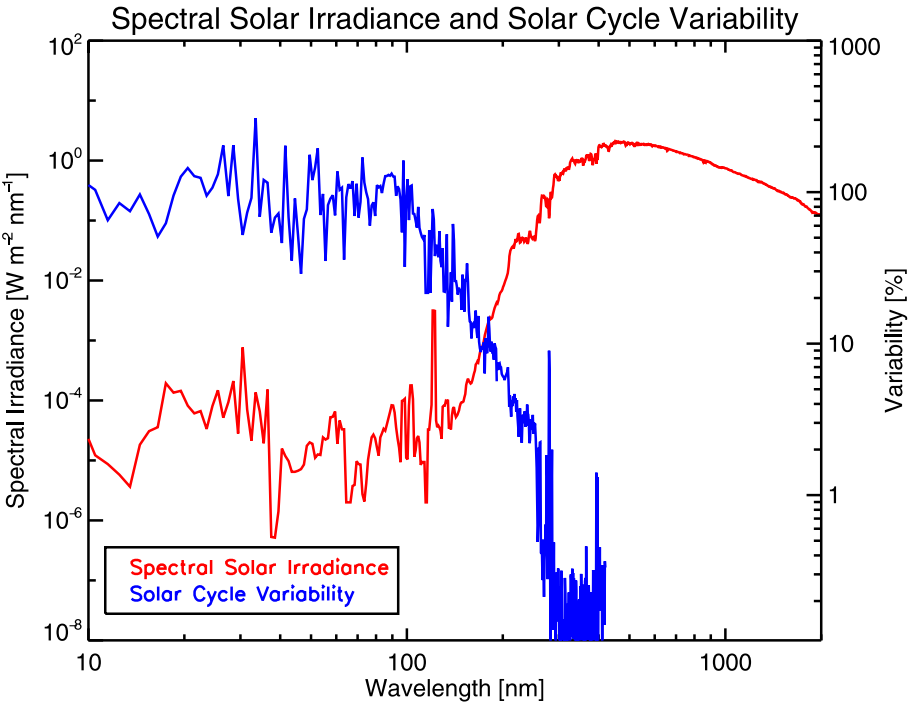

Fig. 2 Although the energy (*red*) at short wavelengths accounts for very little of the total emitted solar radiation, relative variability (*blue*) is greatest at these wavelengths. Data from the Solar Extreme-ultraviolet Experiment (SEE) on TIMED, $\lambda < 191$ nm (Woods et al. 2005a), and from SOLSTICE, UARS Model for $\lambda > 191$ nm (Woods and Rottman 2002)

The XUV Photometer System (XPS), flown on NASA's Thermosphere Ionosphere Mesosphere Energetics Dynamics (TIMED) mission beginning in 2001 and the SOlar Radiation and Climate Experiment (SORCE) launched in 2003, monitors the SSI with 12 filter photodiode photometers (Woods et al. 2005b). The filters define eight wavelength regions from 1 to 34 nm with resolutions ranging from 1 to 10 nm, as well as the highly variable Lyman alpha line (121–122 nm). Nominal cadences are one measurement every 90 minutes from the TIMED/XPS and every 5 minutes from the SORCE/XPS. This instrument's prime function is detecting and analysing high energy solar events with <20% absolute accuracy. The TIMED/XPS data are available from http://lasp.colorado.edu/see/see_data.html and the SORCE/XPS data from http://lasp.colorado.edu/sorce/ssi_data.html.

The Solar Extreme Ultraviolet Monitor (SEM) on the SOlar and Heliospheric Observatory (SOHO) is a photodiode-based transmission grating spectrometer designed to measure the absolute solar EUV flux in the 0.1 to 50 nm region and at the 30.4 nm He II line. The 15-second cadence facilitates near real-time flare monitoring. Data are available from http://www.usc.edu/dept/space_science/instrument_pages/sem.htm.

The Solar X-ray Photometer (SXP) on the Student Nitric Oxide Experiment (SNOE) flew from 1998 to 2003 (Bailey and Korde 2000). The mission's primary purpose was to study Earth atmospheric nitric oxide and auroral emissions, with the SXP providing knowledge of the incident solar radiation at relevant wavelengths. Its five filter-based photodiode photometers had bandpasses covering 2 to 35 nm (Sn: 2–8 nm; Ti: 2–16 nm; Zr/Ti: 5–20 nm;

Al/C: 15–35 nm; and open). The time cadence was one 63-second integrated measurement every 95-minute orbit. Data are available from http://lasp.colorado.edu/snoedata/.

The EUV Grating Spectrograph (EGS) on TIMED was launched in 2001. This Rowland-circle spectrograph covers the spectral range 25 to 200 nm with 0.4 nm resolution. Similar to the TIMED/XPS, this instrument acquires one measurement, in this case a complete spectral scan, during every 95-minute orbit. These TIMED/EGS data are available from http://lasp.colorado.edu/see/see_data.html.

The Solar Mesospheric Explorer (SME) flew from 1981 to 1991. Intended to investigate the processes that create and destroy ozone in the Earth's mesosphere, the spacecraft also contained the Solar Ultraviolet Monitor that provided SSI data from 115 to 302 nm until 1989. This range also gives a Mg II core-to-wing record for the time period. Data are available from http://lasp.colorado.edu/sme_data/.

The Solar Auto-Calibrating EUV/UV Spectrometer (SolACES) on SOLAR/ISS was launched in February 2009 (for details see Schmidtke et al. 2006a, 2006b, and references therein) and consists of four grazing-incidence spectrometers covering the ranges of 16–65, 25–99, 39–151 and 115–226 nm and two ionisation chambers for the absolute calibration. A filter wheel in front of the four spectrometers and the two ionisation chambers allows an internally consistent absolute in-flight calibration over the full spectral range by comparison of selected wavelength bands with the spectrometers and ionisation chambers. Moreover, the irradiance in bands of 17–70 and 100–127 nm, selected by aluminium and magnesium filters can be measured with calibrated silicon diodes at high temporal cadence simultaneously with the spectrometers. The relative standard uncertainty ranges from about 3% to 5% depending on wavelength.

The SOLar and STellar Irradiance Comparison Experiment (SOLSTICE) was first launched on the Upper Atmosphere Research Satellite (UARS) in 1991. This dual grating spectrograph produced a daily mean solar UV spectrum covering 115 to 425 nm with a spectral resolution of 0.2 nm. Special products included in this spectral region include a daily Mg II emission core-to-wing ratio and a daily Lyman-alpha emission product. Data are currently available into 2001 from http://lasp.colorado.edu/uars_data/inst.html.

The SORCE includes two SOLSTICE instruments similar to that flown on the UARS (McClintock and Woods 2005). A slightly narrower wavelength region, 115 to 320 nm, is covered with improved spectral resolution of 0.1 nm. Absolute accuracy, determined by ground calibrations, is better than 5%; relative accuracy, or on-orbit stability, is determined as on the UARS/SOLSTICE by frequent comparisons to an ensemble of stable blue-type stars, giving a stability known to $<0.5\%$/year. SORCE/SOLSTICE data are available beginning in 2003. Currently a gap exists between the UARS/SOLSTICE data and those from SORCE, although these data should be analysed and available in the near future to provide direct overlap between the UARS and SORCE missions. The SORCE/SOLSTICE data are available from http://lasp.colorado.edu/sorce/ssi_data.html.

The Solar Spectrum (SOLSPEC) experiment on SOLAR/ISS launched February 2009 (for details see Thuillier et al. 2003; Schmidtke et al. 2006b, and references therein) measures the solar spectral irradiance from 180–3000 nm. The instrument has a significant heritage from the ones which flew on the ATLAS and EURECA missions. It incorporates three double monochromators using holographic gratings, dedicated to the three spectral domains 180–370, 350–950 and 900–3000 nm, respectively. In-flight photometric calibration is performed by two deuterium and four tungsten ribbon lamps and the wavelength scale is calibrated by a hollow cathode lamp. The relative standard uncertainty ranges from about 1% in the IR/Vis spectral regions up to 3% at 180 nm.

The UARS also included the Solar Ultraviolet Spectral Irradiance Monitor (SUSIM) to monitor solar irradiance in the ultraviolet. This instrument measures SSI from 115 to 410 nm

with 1 nm resolution and 2% relative accuracy. Data were acquired on a daily cadence from 1991 to 2005. One important product from the SUSIM is its Mg II core-to-wing ratio time series. Data are available from http://wwwsolar.nrl.navy.mil/susim_uars_data.html.

The NOAA Polar-orbiting Operational Environmental Satellites (POES) have flown several Solar Backscatter Ultraviolet system/Version 2 (SBUV/2) instruments since 1985. These are scanning double monochromators designed to monitor Earth atmospheric ozone by measuring UV spectral intensities in 12 discrete wavelength bands ranging from 252.0 to 339.8 nm with bandpasses of 1.1 nm. For calibrations, the SBUV/2's also monitor the solar irradiance on a daily cadence by deploying a diffuser plate into the instrument's field of view. In continuous spectral scanning mode, the instruments acquire data from 160 to 400 nm. The SBUV/2 produces a Mg II core-to-wing ratio time series in addition to its spectral solar irradiances. These Level 1B SBUV/2 data are advertised as being available on magnetic tape from the Satellite Services Branch of the National Climatic Data Center (see Sect. 4.4 of the NOAA Polar Orbiter Data User's Guide at http://www2.ncdc.noaa.gov/docs/podug/).

The ESA is similarly flying ozone monitoring instruments with regular solar calibrations. The Global Ozone Monitoring Experiment (GOME) was launched on the ERS-2 in 1995 and provided data until 2003. GOME took SSI measurements from 240 to 400 nm including a Mg II series. Level 1 SSI data are described at http://earth.esa.int/object/index.cfm?fobjectid=1483. The improved GOME-2 was launched on MetOp-A in 2006 and is described at http://www.esa.int/esaLP/SEMTTEG23IE_LPmetop_0.html.

SOHO's Variability of solar IRradiance and Gravity Oscillations (VIRGO) Sun PhotoMeter (SPM) consists of three filter radiometers that monitor the Sun at 402, 500, and 862 nm with bandpasses of 5 nm (Fröhlich et al. 1997). Its position at L1 allows continual solar viewing with measurements reported at a 1-min cadence since early 1996. A redundant SPM allows correction of solar exposure dependent degradation in the primary unit. Daily and hourly SPM averages are available via FTP from ftp://www.pmodwrc.ch/pub/data/irradiance/virgo/SSI/.

The ENVISAT SCanning Imaging Absorption spectroMeter for Atmospheric CHartographY (SCIAMACHY) is similar to GOME. It is an ozone monitoring instrument with regular solar calibrations covering the spectral range from 240 to 2380 nm with a resolution of 0.24 to 1.5 nm. Launched in 2002, its released data currently extend further into the NIR than other SSI instruments. Data are available from http://goes.ngdc.noaa.gov/data/avg/.

The SORCE Spectral Irradiance Monitor (SIM) began operations in 2003. This prism-based spectrometer acquires two spectra per day from 200 to 2700 nm with a resolution between 0.25 and 33 nm (Harder et al. 2005b). A redundant channel allows for degradation tracking with solar exposure. Data are currently available from 310 to 1600 nm from http://lasp.colorado.edu/sorce/ssi_data.html.

Figure 3 gives an overview of these SSI monitors, showing both their time of operation and their wavelength regions covered. Data from several are available through a new and expanding database, the "LASP Interactive Solar IRradiance Datacenter" (LISIRD), at http://lasp.colorado.edu/lisird.

3 Solar Surface Magnetism and its Influence on Radiation

To address the connection between solar surface magnetism and irradiance we review the relevant mechanisms of irradiance variantions and we show how they are applied to photospheric radiative effects by three-dimensional magneto-hydrodynamic simulations of the upper layers of the Sun.

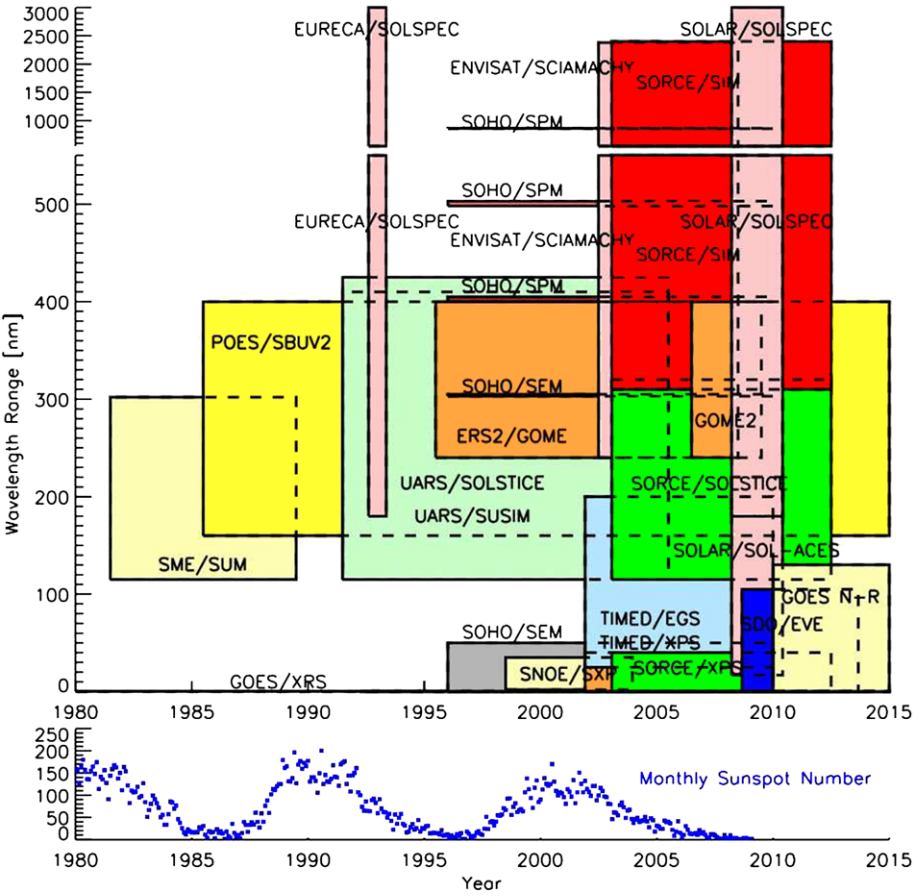

Fig. 3 Complete spectral irradiance measurements of the Sun have only begun recently with the launch of TIMED and SORCE. The LASP Interactive Solar IRradiance Datacenter (LISIRD) provides easy web access to several of the SSI instrument data records discussed here and gives an overview of their performance capabilities

3.1 Mechanisms

Each dark (spot) or bright (facula, network) structure contributes a TSI variation equal to the product of its projected area and its photometric contrast relative to the adjacent, undisturbed photospheric disc. Empirical models reconstruct a TSI variation by adding up these contributions using records of the changing areas of the spots and magnetic brightenings. As we will see in Sect. 5 these models can account for an important fraction of the variance in the irradiance time series.

The observations show that magnetic structures reduce or increase the local radiation flux for as long as they exist at the surface. They present (in the case of sunspots for example) a local magnetic obstruction to the flow of heat through the Sun. One may ask why such a disturbance in the heat flow does not simply readjust ('shunt') around the obstacle. If this were the case it would not cause a TSI variation at all. Several mechanisms that might store (for spots) or release (for the bright component) the energy involved in irradiance variations

have been suggested in response to this conceptual problem. For instance, the 'missing' radiative flux of a spot might, in principle, be stored in intensifying its strong magnetic field (Wilson 1982). But this storage would only occur while the spot's magnetic energy is increasing, whereas the amplitude of sunspot-induced dips in TSI shows no dependence on changes of the spot's area or magnetic field (Zahid et al. 2004).

Modelling of sunspots using current magneto-hydrodynamic codes (Schüssler and Vögler 2006) confirms that their darkness can be understood as thermal 'plugs' in which intense vertical magnetic fields divert heat flow from deeper layers (Spruit 1982; Foukal et al. 1983). Magnetic brightenings act in the opposite sense, as local thermal 'leaks' (Spruit 1977; Deinzer et al. 1984; Chiang and Foukal 1985). They are bright because the effect of their smaller-scale magnetic field is to form small depressions in the photospheric surface, enabling radiation from lower and hotter atmospheric layers to escape more easily (Spruit 1976; Spruit 1977). These depressions have now been imaged directly in the highest-resolution pictures of the photosphere (Lites et al. 2004) and are reproduced in detail by realistic 3-D radiative magneto-hydrodynamic simulations of these small magnetic structures (Keller et al. 2004; Carlsson et al. 2004; Steiner 2005).

Calculations with such a thermal impedance model of solar luminosity variation show that the heat flux diverted by a spot is not merely shunted aside to reappear nearby. Instead, the thermal perturbation spreads horizontally and back down into the Sun, much more quickly than it can be radiated from the photosphere. As a consequence, the 'blocked heat flux' effectively remains stored in the Sun for hundreds of millennia instead of appearing elsewhere on the surface, in agreement with the observation that 'bright rings' around spots are weak or absent (Fowler et al. 1983; Rast et al. 1999). This rapid redistribution is also in agreement with the absence of 'thermal shadows' preceding spot emergence (Foukal and Fowler 1984), and the absence of phase differences between the irradiance dip and the appearance of a spot's magnetic field at the photosphere (Foukal et al. 1983). The thermal plug model predicts that the Sun's irradiance immediately drops by a factor equal to the product of the spot's cross-sectional area and its brightness deficit, as observed. This factor is independent of the spot's growth or decay, also in agreement with observations (Zahid et al. 2004). The heat missing from the spot is stored as slightly increased internal and potential energy of the entire solar convective envelope. The predicted changes in solar radius accompanying changes in spot area are unobservably small (Spruit 1982). This is consistent with the increasingly tight upper limits on measured radius variations (Antia 2003; Kuhn et al. 2004), but conflicting with Sofia (1998, 2004), Egidi et al. (2006), Noël (2005).

The Sun's remarkable ability to store, rather than quickly re-radiate, fluctuations in heat flow to the photosphere can be understood in terms of a simple illustration. Consider a satellite in temperature equilibrium with its surroundings in space. Then imagine a resistor on the satellite is briefly turned on, sending a heat pulse through the satellite at a rate determined by the thermal diffusivity of aluminium. New isotherms describing the somewhat warmer temperature distribution within the satellite will be relatively quickly established over this diffusive time scale. But the satellite is now warmer than before, and must eventually return to equilibrium with its space surroundings by radiating the heat liberated by the resistor. For a satellite, this time scale for radiative equilibration is a couple of orders of magnitude longer than the diffusive time scale, and until it is achieved, the resistor's heat pulse is stored in the satellite.

The solar equivalent of the thermal diffusion in a metal is thermal exchange by convective flows. The radiative equilibration time scale of the Sun's convection zone, about 100,000 years, is about 6 orders of magnitude longer than this exchange time scale by convective flows, and storage of thermal disturbances is much more efficient than in the metal analogy.

As a consequence, neither the excess emission in the bright magnetic component nor the darkness of spots is expected to be compensated by measurable changes in photospheric temperature elsewhere on the disc.

These findings were originally obtained from calculations in which convection was approximated by turbulent diffusion. 3-D hydrodynamical simulations, which accurately reproduce observation of solar convection near the photosphere (Rosenthal et al. 1999) confirm the picture sketched above, of the Sun's convective envelope as a 'thermal superconductor' with a huge thermal inertia (Spruit 1991). Interestingly, the same thermal inertia that makes possible the irradiance fluctuations due to 'superficial' photospheric magnetic structures, also explains why additional variations with origin deeper in the Sun have not been observed so far.

3.2 Local MHD Simulations

Realistic radiative MHD simulations of photospheric magneto-convection provide a means to study the interaction between magnetic features, convective flows and radiation in detail. In connection with solar irradiance variations, such simulations serve a twofold purpose: Firstly, they allow us to investigate the physical mechanism behind variations in photospheric brightness and radiation flux, thus providing the theoretical underpinning and quantitative understanding of the relation between surface magnetism and irradiance. Secondly, solar surface simulations for a range of magnetic fluxes (from 'quiet' Sun to strong plage) yield information about the photometric properties of solar surface fields and may provide improved input parameters for irradiance models.

State-of-the-art radiative MHD simulations of photospheric magnetoconvection (e.g., Bercik et al. 2003; Vögler et al. 2005; Stein and Nordlund 2006) have reached a high level of realism and have been very successful in reproducing and explaining surface features like G-Band bright points (Schüssler et al. 2003; Shelyag et al. 2004) or facular brightenings (Keller et al. 2004; Carlsson et al. 2004; De Pontieu et al. 2006). In what follows, we consider a series of radiative MHD simulations ranging from nonmagnetic convection to magnetoconvection under conditions corresponding to strong plage and analyse the dependence of average photometric properties, including the emergent radiation flux and center-to-limb variation of intensity and facular contrast, on the average magnetic flux density. Some of these results have been presented previously by Vögler (2005).

3.2.1 Simulation Runs

The MURaM code (Vögler 2003; Vögler et al. 2005) has been used for these simulations. It integrates the time-dependent MHD equations for a compressible, partially ionised plasma and includes a nongrey LTE radiative transfer based on multigroup frequency binning.

The results analysed here are based on five simulation runs with varying amount of net vertical magnetic flux threading the computational domain: a nonmagnetic reference run and four magnetic runs. The magnetic runs were started by introducing a homogeneous, vertical magnetic field of strength B_0 into fully developed convection. The values chosen for B_0 are 50 G (comparable to quiet Sun network), 200 G, 400 G (typical values for plage regions), and 800 G. In all cases the simulation domain included the surface of continuum optical depth unity at 500 nm and extended 6 Mm in both horizontal directions and 1.4 Mm in the vertical direction. A detailed description of the boundary conditions is given in Vögler (2005). It is important to point out that a fixed entropy density of the fluid entering the simulation domain from below was specified, letting the total energy flux through the

system adjust itself according to the conditions of a given simulation run. Any dependence of the brightness on the amount of magnetic flux is thus solely due to the action of surface magnetic fields. Since the entropy throughout the up-flowing parts of the convection zone is essentially constant, with inhomogeneities efficiently smoothed out by the strong expansion of rising fluid parcels in a strongly stratified system (Nordlund et al. 1997), the entropy density was assumed to be uniform across the up-flow regions at the lower boundary and independent of B_0. The value of the entropy was chosen such that the radiative energy flux of the nonmagnetic run on average equals the solar value of $F_\odot = 6.3 \times 10^{10}$ erg cm^{-2} s^{-1} to within a percent.

Figure 4 gives an impression of the morphology of photospheric magnetoconvection for different values of the average magnetic field strength. The upper row shows the largely

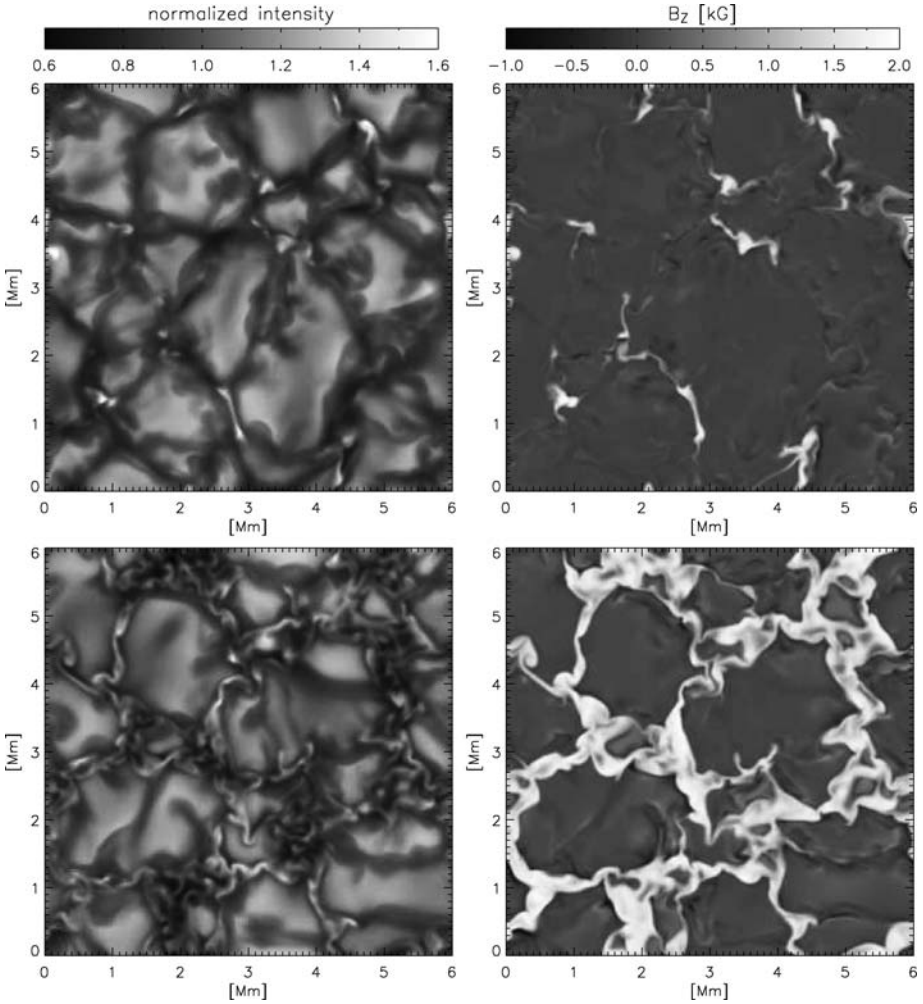

Fig. 4 *Left column*: Maps of bolometric brightness for representative simulation snapshots with $B_0 = 50$ G (*top*) and 400 G (*bottom*). The same greyscale was used for both maps. *Right column*: corresponding horizontal cuts of the vertical magnetic field strength near $\langle \tau_{500} \rangle = 1$. Strong fields appear *white*, *dark grey* regions are essentially field-free

undisturbed granulation pattern (left) and the distribution of the vertical magnetic field in a horizontal cut near $\langle\tau_{500}\rangle = 1$ (right) for the simulation with $B_0 = 50$ G. The lower panels show the corresponding maps for $B_0 = 400$ G representing strong network or plage regions. In this case, the granulation appears disturbed, with on average smaller granules ("abnormal granulation"). Most of the magnetic flux has been swept into the intergranular downflow network, where it reaches field strengths of up to 1.5–2 kG near the visible surface of optical depth unity.

The simulation with $B_0 = 800$ G (not shown in Fig. 4), exceeds the typical average field strengths of solar plage and represents the transition to the magnetically dominated regime of magnetoconvection. At the far end of the range of average field strengths one reaches the regime of pores and sunspot umbrae (e.g., Cameron 2005; Schüssler and Vögler 2006), which is outside the scope of the simulations discussed here.

3.2.2 Radiation Analysis

The left panel of Fig. 5 shows the angle-integrated bolometric radiation flux at the top of the computational domain (i.e. the energy per unit area and unit time radiated by the model) averaged over space and time as a function of the average magnetic field strength B_0 in the five simulation runs. For the cases with $B_0 = 50$, 200, and 400 G, the radiation flux is larger than in the nonmagnetic run, the flux excess reaching a maximum of approximately 2.5% for the 200 G run. In the 800 G case, on the other hand, the radiation flux is reduced by about 4.5%.

The bolometric brightness at disk center (right panel of Fig. 5) is enhanced by approximately 1% for the cases with $B_0 = 50$ and 200 G. For larger B_0 the values drop clearly, reaching a brightness reduction of 10% for the 800 G case. In general, for all four magnetic runs the normalised disk-center intensities appear to have lower values than the normalised flux integrated over the upper hemisphere, indicating a modified angular dependence of the radiative energy transport, as is discussed in more detail below.

In order to gain insight into how the brightness variations come about, Vögler (2005) decomposed the disk-center brightness maps into three constituents, based on field strength

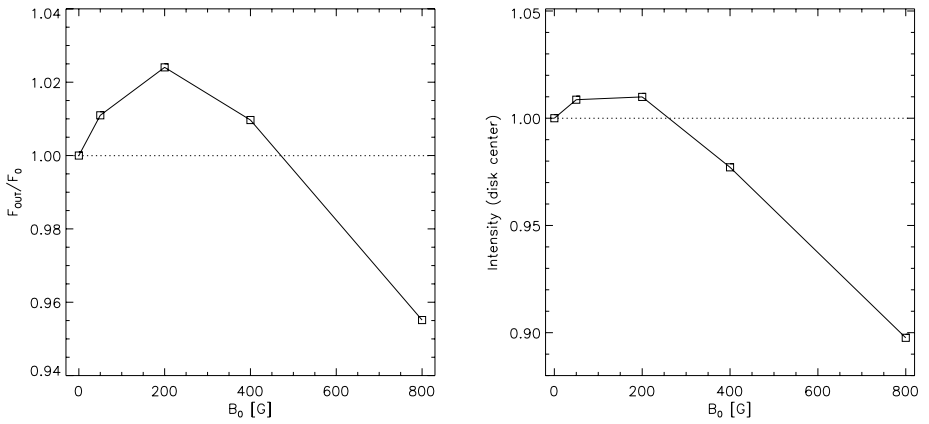

Fig. 5 Spatio-temporal average of the outgoing (angle-integrated) bolometric radiation flux (*left panel*) and of the bolometric disk-center intensity (*right panel*), as a function of the average field strength, B_0. Both *curves* are normalised with the values for the non-magnetic case. From Vögler (2005)

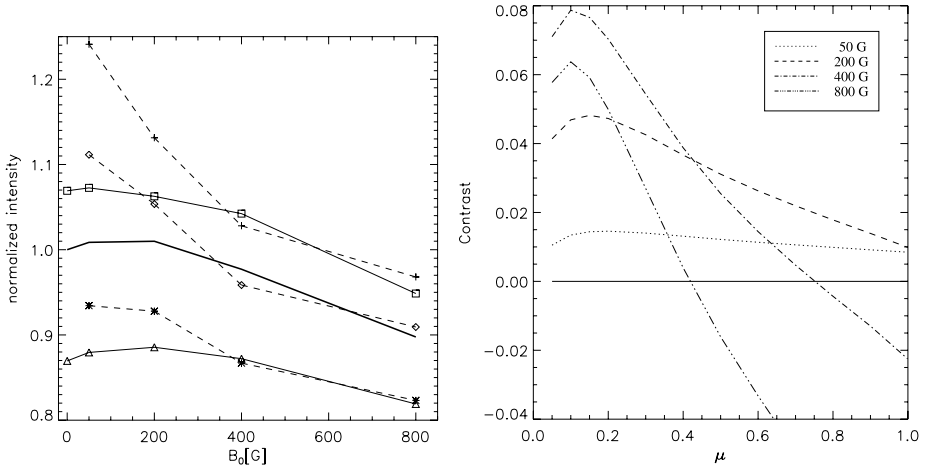

Fig. 6 *Left panel*: Average disk-center intensity as a function of the average field strength B_0. *The curves* correspond to averages taken over granules (*solid line, squares*), downflow lanes (*solid line, triangles*), regions with 500 G $< B_z <$ 1000 G (*dashed, asterisks*), and regions with B_z exceeding, respectively, 1.0 kG (*dashed, diamonds*), and 1.5 kG (*dashed, crosses*) at $\langle\tau_{500}\rangle = 1$. *The thick solid line* shows the average over the whole area (same as Fig. 5, right panel) for comparison. All values are relative to the average disk-center intensity of the non-magnetic run. *Right panel*: Center-to-limb variation of the contrast, $(I(\mu) - I_0(\mu))/I_0(\mu)$, where $I_0(\mu)$ is the angle-dependent intensity of the nonmagnetic simulation run, for five simulation runs with an average field strength of 0 (*solid line*), 50 G (*dotted*), 200 G (*dashed*), 400 G (*dash-dotted*), and 800 G (*triple-dot-dashed*)

and vertical velocity at a height level corresponding to $\langle\tau_{500}\rangle = 1$: granular up-flows (areas with $|B_z| <$ 500 G and $v_z > 0$), intergranular downflow lanes ($|B_z| <$ 500 G and $v_z < 0$), and magnetic flux concentrations ($|B_z| >$ 500 G). Figure 6 shows the average brightness of granules, lanes and magnetic fields, all taken relative to the average brightness of the nonmagnetic simulation run. For the 50 G and 200 G cases, the brightness of granules is only weakly affected by the magnetic field. However, for $B_0 >$ 50 G there is a decrease of granule brightness which amounts to about 10% for the simulation with $B_0 =$ 800 G. The darkening of granules with increasing average field strength can be understood as a result of hampered convective energy transport in the presence of magnetic fields.

So, the inhibition of the convective energy transport by magnetic fields has a significant effect on the radiative energy output for photospheric regions with average flux densities beyond 200 G. The brightness of downflow lanes in the 50, 200, and 400 G cases is somewhat larger than in the case $B_0 = 0$. According to Vögler (2005) this may be due to the fact that in the upper photosphere the line of sight of downflow lanes partially runs through the partially evacuated, optically thin magnetic canopy which fans out with height. As a result one can look into deeper, hotter layers, similar to the hot wall effect that leads to facular brightenings (Spruit 1976; Keller et al. 2004). For $B_0 >$ 200 G the lane brightness follows the systematic downward trend of the granules.

The three dashed curves in Fig. 6, left panel, show the average brightness of magnetic flux concentrations with, respectively, 500 G $< B_z <$ 1000 G, 1000 G $< B_z <$ 1500 G, and $B_z >$ 1500 G. Independently of B_0, one finds that the average brightness of magnetic patches increases with increasing field strength of the flux concentrations, i.e. for any given value of B_0 the strongest fields appear brightest.

This results from the fact that the level of optical depth unity is depressed in regions of strong field because of the higher degree of evacuation, thus exposing hotter material. All three curves exhibit a clear downward trend with growing B_0. This can be understood as a consequence of the tendency of magnetoconvection to form larger magnetic structures as the average flux density increases. The radiated energy coming from magnetic structures is mainly supplied by lateral channelling of hot-wall radiation (convective transport inside the strong fields is negligible). With growing filling factor and size of strong field features, the thermal structure of strong fields has to adjust in order to maintain a balance between the horizontal energy input through the walls and the radiative losses in the vertical direction, resulting in lower brightness. As a comparison with the brightness averaged over the whole area (thick line in Fig. 6, left panel) shows, flux concentrations with field strengths larger that 1.5 kG on average stand out as bright features for all values of B_0. For the 50 G and 200 G cases, the values for kilogauss fields significantly exceed the average "quiet Sun" ($B_0 = 0$) disk-center brightness.

The different dependence on B_0 of radiation flux and disk-center intensity is indicative of a modified angular distribution of the radiation field in the presence of a magnetic field (the hot wall effect). The center-to-limb variation (CLV) of the contrast, defined as $(I(\mu) - I_0(\mu))/I_0(\mu)$, with $\mu = \cos\theta$, where θ is the heliocentric angle, and $I_0(\mu)$ is the angle-dependent intensity of the nonmagnetic model, is shown in Fig. 6, right panel. Obviously, the CLV of the contrast depends strongly on the amount of magnetic flux in the simulation. For small B_0 the contrast varies relatively weakly with μ and is always positive. For large B_0 the contrast is negative at disk center, grows strongly as a function of μ and is positive near the limb. Over a large range of values for B_0 the maximum contrast obtained increases with B_0. Beyond $B_0 = 400$ G it drops again but seems to be less sensitive to a further increase of the average magnetic field strength. The picture obtained by Vögler (2005) exhibits many qualitative similarities with the MDI-based contrast measurements by Ortiz et al. (2002). The most striking difference is the heliocentric angle where the maximum contrast occurs. In the simulations discussed here, the contrast increases monotonically up to at least $\mu = 0.2$ for small B_0 and continues growing towards the limb for large B_0, while the contrasts in the study by Ortiz et al. (2002) generally reach their maximum closer to disk center. A possible explanation for this discrepancy may lie in the fact that in the latter study the magnetic field strength is extracted from the magnetogram signal averaged over a MDI pixel which carries no information about the spatial distribution of magnetic flux within the resolution element. Thus different magnetic configurations with the same magnetogram signal but potentially very different CLV are grouped into the same field-strength bin, which may have a levelling effect on the contrast. One should also keep in mind that the CLV of the contrast may be wavelength dependent, so the comparison of synthesised bolometric intensities with results based on MDI continuum measurements should be cautioned.

In summary, the finding that the radiative energy output in simulations of plage or facular regions is significantly enhanced supports the hypothesis that surface magnetism is a main cause of short-term solar irradiance variations.

4 Semi-Empirical Atmosphere Models

In order to calculate realistic radiation (radiances) from structures in the solar atmosphere, which correspond to the known magnetic and non-magnetic sources of radiative variability distributed across the visible solar surface, thermodynamic and compositional information on each of these structures are required. We review the current one-dimensional radiative

transfer approaches which do not explicitly include the effects of magnetic fields in a self-consistent manner but instead determine the atmosphere based on semi-empirical procedures.

4.1 Model Atmospheres

To our knowledge, currently all solar atmosphere models used in spectral synthesis calculations as part of the irradiance modelling are one-dimensional semi-empirical models. The models essentially describe the temperature and density structure of each solar component as a function of height (or optical depth). Additionally, other physical parameters, such as number densities of various species and turbulent velocities can also be provided. The functional dependence of these quantities is adjusted so as to achieve reasonable fits to observed line and continuum intensities.

These model atmospheres go back to the work of Vernazza et al. (1981) with considerable modifications by Fontenla et al. (1990, 1991, 1993). Built on these models are the so-called 'RISE' (Radiative Input from Sun to Earth) models which extend from the solar photosphere into the transition region based on the work by Fontenla et al. (1999). The RISE models were recently updated by the SRPM models Fontenla et al. (2006, 2007). Additionally, Avrett and Loeser (2008) have updated 1D atmosphere models for the averaged quiet Sun.

The most common atmosphere models currently available are coded by the letters as follows:

A: the cell centre faint component of the quiet Sun,
C: the average median intensity quiet Sun component,
E: the bright network component of the quiet Sun,
F: the enhanced network component for the active Sun,
H: the faint plage component for the active Sun,
M: medium brightness plage component for the active Sun,
P: the bright plage (faculae) component for the active Sun,
R: sunspot penumbra, and
S: sunspot umbra.

The more general set of radiative equilibrium model atmospheres by Kurucz (1991, 1993), hereafter Kurucz, correspond to a particular effective temperature, chemical abundance, and gravity for an atmosphere in radiative equilibrium and thus does not include a chromosphere and transition region.

As a basis for various spectral synthesis calculations we group the representation of these structures into quiet Sun, and those leading to radiation deficits and excesses (see next section). It is important to keep in mind that different research groups utilise different numbers, combinations and modifications of the model atmospheres, listed in Table 1.

4.1.1 Quiet-Sun Model Atmospheres

The two most commonly used quiet-Sun models in the literature are RISE C (Fontenla et al. 1999) and the solar model by Kurucz. E.g., the SATIRE quiet Sun model is based on the model atmosphere of Kurucz (1991) in radiative equilibrium with an effective temperature of 5777 K. Haberreiter et al. (2008a) use the RISE C model and validate the results employing the quiet Sun Kurucz model. The RISE C model is also used by Penza et al. (2004). Fontenla et al. (1999, 2006) use Model C (most recently Model B), D and E for the quiet Sun irradiance, i.e. a combination of 3 components.

The agreement between the observations and the model calculations is good overall, in particular in the visible. For wavelengths between 450 and 1050 nm, e.g., Unruh et al. (1999) determine a deviation of less than 0.7% between the disk-centre intensity calculated with ATLAS9 from the Kurucz quiet-Sun model and the observations of either Burlov-Vasiljev et al. (1998) or Neckel and Labs (1984). This is indeed comparable to the deviation between the two sets of measurements. Haberreiter et al. (2008a) find a good agreement between the quiet Sun spectrum in the UV and SOLSTICE observations, whereas Fontenla et al. (2006) get a good agreement with observations in the IR.

The centre-to-limb variations calculated from these model atmospheres generally agree well with the observations for a large range of wavelengths and have been discussed in Unruh et al. (1999), Penza et al. (2004) and Fontenla et al. (2006). Some discrepancies, however, remain for intensities derived from RISE C and Kurucz's quiet-Sun models, in particular at UV and IR wavelengths (see Fig. 4 in Fontenla et al. 2006).

4.1.2 Sunspots and Pores

Much of the original work on sunspot model atmospheres goes back to Maltby et al. (1986) and Kjeldseth-Moe and Maltby (1969) for sunspot umbrae and penumbrae respectively. Maltby et al. (1986) suggested that sunspot umbrae vary with the solar cycle and proposed three different umbral models (but see Mathew et al. 2007, who found no support for this in MDI data). Their model M formed the basis for RISE S, the sunspot model atmosphere proposed by Fontenla et al. (1999). With model R, a penumbral atmosphere was only added very recently to the set of RISE models (see Fontenla et al. 2006). The choice of a sunspot model particularly affects short-term reconstructions and relatively large variations can be seen between different irradiance reconstructions in the literature. Haberreiter et al. (2005) employed the RISE S model for the reconstruction of the UV spectrum. Penza et al. (2003) experimented with using a Kurucz's stellar atmosphere at 5150 K to model the combined sunspot penumbra and umbra (see also Fligge et al. 2000), but settled on a method of scaling intensities calculated from the RISE quiet-Sun model according to the umbral and penumbral contrasts measured by Tritschler and Schmidt (2002). In the SATIRE models (see, e.g., Krivova et al. 2003; Wenzler 2005; Wenzler et al. 2006), the sunspot penumbral fluxes are calculated from similar but cooler model atmospheres with effective temperatures 5250 K or 5400 K (Unruh et al. 1999). The sunspot umbra is also in radiative equilibrium with an effective temperature of 4500 K.

Testing sunspot model atmospheres and the resulting intensity calculations is non-trivial for a number of reasons. One of these is that detailed spectral calculations that include all the metallic lines as well as molecular lines and opacities become more complex and time consuming as cooler effective temperatures are reached. Another reason is that observational data are hard to obtain as most sunspot spectra are affected by stray light. While correcting for stray light is possible over limited wavelength ranges, no 'flux-calibrated' sunspot spectrum is currently available. As a consequence, most authors consider their sunspot models as being somewhat preliminary.

4.1.3 Bright Components

Given the large surface area covered by small-scale magnetic features and their important role in solar variability, especially on time scales of years to decades, it is somewhat irksome that the uncertainty over their temperature and density structure is arguably even greater than for sunspots. It is here, also, that the commonly used assumption of a plane-parallel 1-D

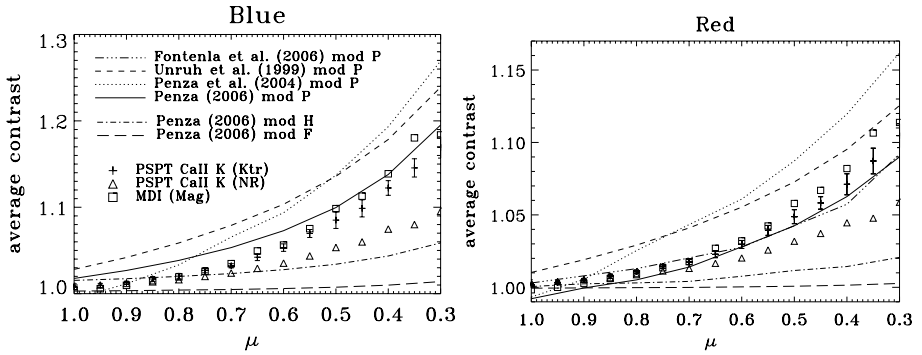

Fig. 7 Comparison of contrast CLV of facular regions measurements with output of semi-empirical atmospheric model computations (*left* = PSPT Blue band (409.6 nm), *right* = PSPT Red band (607.2 nm)). The different lines show the results of model computations. Symbols represent the results obtained for the year 2000 by three different identification methods, based on PSPT Ca II K images and on MDI magnetograms. For clarity, deviation of measured values are plotted only for the results obtained with the PSPT Ca II K *Ktr* method. Adapted from Ermolli et al. (2007)

model atmosphere is harder to justify (see Sect. 3.2). Most authors differentiate between a number of different small-scale features. Fontenla et al. (2006), e.g., use 4 different bright models, ranging from relatively low-contrast network components (model E), via F and H up to 'bright plage', model P, which was originally based on Lemaire et al. (1981). Note that 'bright plage' means plage seen in white light, which therefore actually corresponds to faculae.

An alternative approach has been adopted by Krivova et al. (2003) and Fligge et al. (2000) for SATIRE models where only one facular atmosphere is used, but the facular filling factor for each pixel is scaled according to the magnetic flux of that pixel. The latter facular model atmosphere uses model P of Fontenla et al. (1993) as a starting point. However the original model has been altered for use in LTE with ATLAS9 in order to achieve better agreement with observations and to optimise irradiance reconstructions (Unruh et al. 1999). These modifications consist mainly of a truncation of the original atmosphere before the temperature minimum and an extrapolation down to slightly lower temperatures in order to mimic the NLTE source function of stronger lines to first order.

It is well known that a large range of flux tube sizes are present on the solar surface. What is less well understood is how their contrasts vary with size and limb angle over a large wavelength range. A number of comparison data sets are available (see, e.g., the discussion in Unruh et al. 1999), though only a few of them measure contrast, wavelength and size/magnetic field strength simultaneously. As an example of the available observations and adjustments needed for these model structures, Fig. 7 shows a comparison between computed and measured contrasts in the blue (left panel) and red (right panel) PSPT bands (409.6 and 607.2 nm central wavelengths respectively) with position across the solar disk (μ = cosine of the heliocentric viewing angle; $\mu = 1$ is disk centre). "PSPT" stands for Precision Solar Photometric Telescopes (PSPT) located at Mauna Loa and Rome (Coulter and Kuhn 1994). The differences in the lines of different colours show clearly that there are large differences in the model atmospheres adopted for the calculation of solar irradiance variations. Comparing the different lines which represent the facular contrast calculated from a variety spectral synthesis approaches using different model atmospheres, to the symbols which are the observed continuum facular contrasts identified by three different methods

(see caption for details), illustrates the influence of the feature identification method, especially when approaching the limb.

4.2 Radiances of Atmosphere Structures

While we consider a detailed discussion of all available spectral line and continuum synthesis codes to be beyond the scope of this paper, we list those most commonly used, along with the selection of model atmospheres, in the calculation of solar radiances (specific intensity as a function of wavelength and position on the solar disk) in Table 1. In Sects. 5.3 and 5.2 we review how these radiances are combined with time dependent information on the distribution of solar magnetic structures to estimate irradiances.

In the SATIRE approach, all fluxes (Unruh et al. 1999) calculated from these atmospheres depend on wavelength, but are time-independent. The wavelength dependent fluxes are obtained from intensity spectra using the ATLAS9 program (Kurucz 1991) with opacity distribution functions, in the LTE approximation. These fluxes allow a reconstruction of either solar spectral irradiance (for wavelengths between roughly 200 nm and 160 μm) and total solar irradiance (by integrating over all the computed wavelengths). In the current version of SATIRE, the solar atmosphere is represented by a 4-component model.

Penza et al. (2003, 2004) use the Fontenla et al. (1999) model atmospheres, with the SPECTRUM program (Gray and Corbally 1994), under the LTE approximation. Under this approximation, the original Fontenla et al. (1999) models were altered in analogy to the procedure of Unruh et al. (1999), with a truncation at the temperature minimum and a linear extrapolation down to lower temperatures. Similar computations have also been performed assuming the most recent atmospheric models proposed by Fontenla et al. (2006). This suite of models uses the solutions of radiative transfer and of statistical equilibrium with a non-LTE treatment. As described in Sect. 5.2 these models were used e.g. by Fontenla et al. (2004) and Harder et al. (2005a) to reconstruct the solar radiation output measured by SORCE/SIM.

Haberreiter et al. (2005, 2008a) make use of the spherical, NLTE radiative transfer code COSI (Table 1) to calculate intensity spectra of solar features based on the model atmospheres published by Fontenla et al. (1999). Thus, they account for the rising temperature profile of the chromosphere, essential for the calculation of realistic synthetic UV spectra (Haberreiter et al. 2002).

Table 1 All models indicated by single letters are RISE models, as presented in Fontenla et al. (1999). The prefix KUR indicates Kurucz's hydrostatic equilibrium LTE models as available from Kurucz (1993)

Authors	Synthesis program	Quiet Sun	Dark component(s)	Bright component	Network
Fontenla et al.	SRPM	A, C, D, E	S, R	F, P, H	E, F
Krivova et al. (SATIRE)	ATLAS9	KUR asun	KUR 4500 K, 5250 K & 5400 K	modified RISE P scaled with magnetic flux	as for faculae
Penza et al.	SPECTRUM	C	KUR 5150 or scaled C	P (truncated)	E (truncated)
Fox et al.	SunRISE	C	S, A	F, H, P	
Haberreiter et al.	COSI	C	S	P	

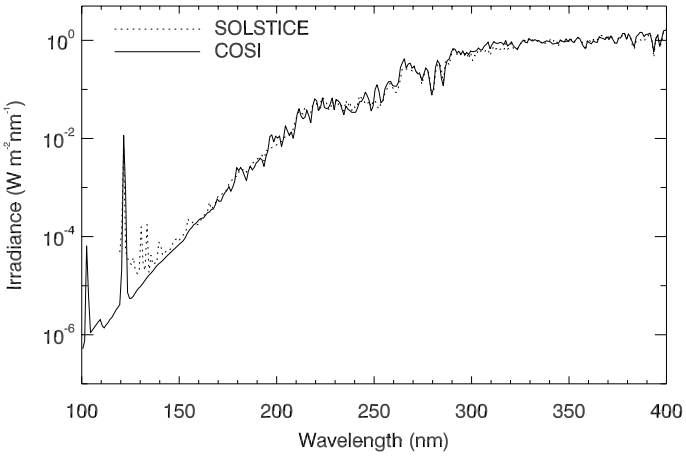

Fig. 8 Comparison of the COSI NLTE calculation using the RISE model C with SOLSTICE observations; adopted from Haberreiter et al. (2008a)

Radiative equilibrium atmosphere models that do not feature the temperature rise lead to substantial differences in the UV between the synthetic spectrum and observations (see e.g. Fig. 17). In contrast, including the chromosphere leads to a reasonable agreement between the model calculations and observations, as shown in Fig. 8. The remaining disagreement between the calculated spectrum and the observation in the UV could be due to incomplete atomic data and missing opacity contributions.

It might be noted here that the UV radiation causes the metals to ionise and consequently affects the electron density, which in turn has a direct consequence on the population number of the negative hydrogen ion; being the dominant opacity source of the infrared (IR) and very sensitive to the electron density. Thus, the UV and the IR can only be calculated correctly if the ionisation of the metals and the negative hydrogen are calculated self-consistently. As the UV is strongly influenced by the line blanketing it is also essential to account for all relevant line opacities. The ATLAS9 code for example accounts for the line opacities by means of opacity distribution functions. Haberreiter et al. (2005, 2008a) account for the line blanketing by introducing iterated NLTE opacity distribution functions, *NLTE-ODFs*, into the radiative transfer calculation. The SunRISE and SRPM account for each single line in the radiative transfer calculation (Fontenla et al. 1999).

In contrast to the ATLAS9 code and SRPM, which calculate the radiances in plane-parallel symmetry, COSI is setup in spherical symmetry, allowing calculations for rays at and beyond the solar limb Haberreiter et al. (2008b). The higher the emergent intensity is formed in the solar atmosphere, the more important is the contribution of the rays beyond the solar limb to the irradiance. Therefore, this becomes increasingly important for shorter wavelengths, i.e. UV and EUV, as they are formed higher up in the atmosphere. In de EUV, however, the structure of the upper atmosphere, e.g. the presence of loops, must be taken into account.

All of the atmospheres used for solar radiance calculations have to be seen as average models, both in the time and spatial domain, as they neglect solar oscillations and small-scale features. They are models for the solar atmosphere as observed at moderate spatial and temporal resolution (approx 3″ and approx 30 minutes, respectively) (Fontenla et al. 2006). Being one dimensional, they can also not account for the shape of the magnetic flux tubes,

which leads to discrepancies in flux-tube contrasts near the limb. The errors introduced through these discrepancies tend to be small, due to the small contribution of regions near the solar limb to the total flux. However, when modelling high spatial-resolution (non disk-integrated) data, more complex 3-D models need to be invoked (see, e.g. Solanki et al. 2006 for a review, see also the discussion in Sect. 3.2).

5 Reconstructions of Irradiance Variations

In Sects. 3 and 4 we have described the physical ideas regarding the variation of TSI and detailed physical effects describing how magnetic features influence the emerging intensity. These results can be used as the basis for detailed reconstructions of irradiance in order to either test the physical models or to extend the irradiance record beyond the period of time for which measurements are available.

Such reconstructions have been carried out at different levels of sophistication. We first discuss the simpler ones based on indices of irradiance followed by the more advanced, that make use of model atmospheres.

5.1 Irradiance Reconstruction from Indices

Different regions of the solar spectrum arise from radiation formed in different solar atmospheric layers. Since magnetic fields change the temperature and density by different amounts in different atmospheric layers, observing the Sun at selected wavelengths or wavelength regions formed over a range of temperatures provides a tool for detecting and quantifying the impact of solar activity throughout the solar atmosphere, and hence on the emergent radiation at many wavelengths. Particularly useful in this regard are solar emission and absorption lines whose cores form above the temperature minimum, i.e. in the chromosphere. This is the case for the Mg II h and k and Ca II H and K doublets. When measured as an average over the disk (Sun-as-a-star observations), ratios of the core emission relative to the wings of such spectral features yield information about the prevailing global temperature structure pertaining to an area-weighted average of the distributions from specific magnetic features. Figure 9 compares the variations in several indices of solar activity that have been widely used to infer irradiance variations. The sunspot number, which is a visually determined, numerical rather than physical index, is the longest available direct indicator of solar activity. The 10.7 cm radio flux (Tapping and Detracey 1990) reflects a combination of chromospheric (longer term) and coronal (short term) influences of solar activity and it is highly correlated with the sunspot number. The Mg II index is the core-to-wing ratio of the Mg II doublet at 280 nm (Heath and Schlesinger 1986) and the data used here is an updated version of the composite by Viereck et al. (2004) (originally from ftp://ftp.ngdc.noaa.gov/STP/SOLAR_DATA/SOLAR_UV/NOAAMgII.dat, and updated since 2003 from http://lasp.colorado.edu/sorce/data/mgii_product.hml). This chromospheric index tracks closely the flux variations in the equivalent width of the He I line at 1083 nm and the core of the Ca II K emission at 393 nm. It is a good proxy for brightening due to faculae and network.

Information about the primary sources of irradiance variability, sunspots, faculae and network is available from a variety of solar observations which enable the quantitative modelling of irradiance variability independently of direct measurements. Sunspot darkening, the fractional change in irradiance caused by sunspots is described by the Photometric Sunspot

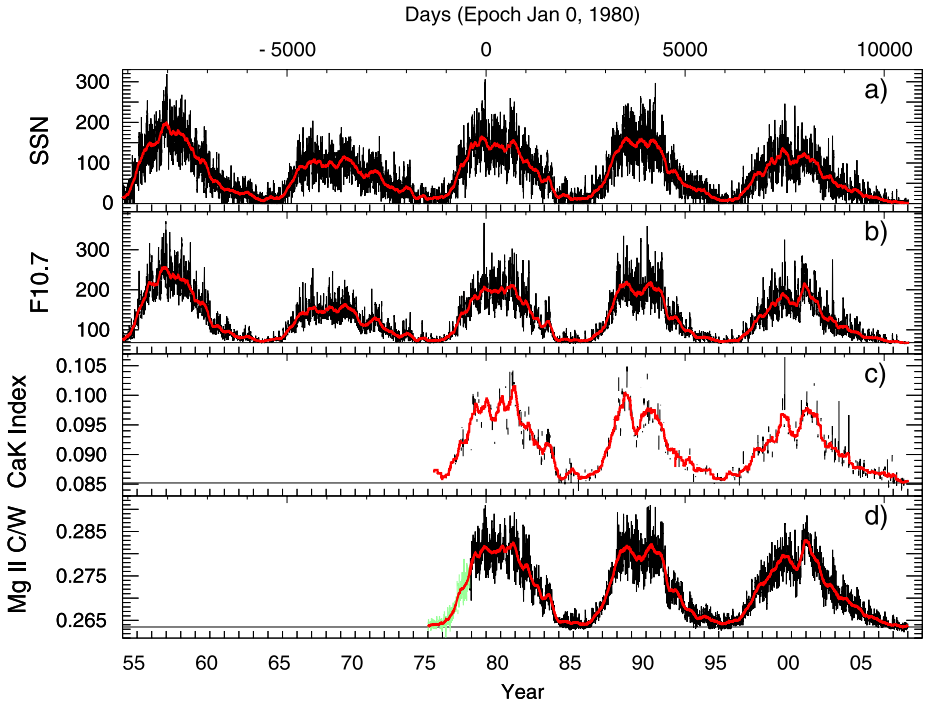

Fig. 9 Time series of daily values of four solar activity indices that have been used in various ways to infer solar irradiance variations. The sunspot number (SSN) in (**a**) is a generic indicator of solar activity, available since 1610. The radio flux at 10.7 cm (F10.7) in (**b**) is available since 1947, and primarily reflects brightness changes in the corona. The Ca-K 1 Å full-disk index form Kitt-Peak in (**c**) and the Mg II index in (**d**) represent chromospheric activity. The Mg-II data before 1978 are from He-I observation at Kit-Peak, scaled to Mg-II by a regression analysis during cycle 21. These chromospheric indices closely simulate changes in global brightness associated with faculae, plages and network

Index, PSI or P_S, proposed in 1981 by Hudson et al. (1982), is calculated explicitly (in this case for total irradiance) as

$$P_S = \sum \Delta S/S_Q = \sum \mu A_{WDC}(C_S - 1)\frac{R(\mu)}{\int_0^1 R(\mu)\mu d\mu}, \quad (1)$$

where ΔS is the reduction in irradiance relative to the quiet Sun, S_Q, for a sunspot of area A_{WDC} (in fractions of the solar hemisphere) at location μ in heliocentric coordinates. C_S is the sunspot's contrast (ratio of spot emission to the background quiet photosphere) and $R(\mu)$ is the centre-to-limb variation function which is assumed to be the same for the quiet photosphere and the spot. The summation is over all spots on the solar disk at a specific time. It utilises the bolometric contrast and center-to-limb functions as e.g. Eddington limb darkening $R(\mu) = (3\mu+2)/5)$ or more detailed functions (from e.g. Chapter 14.7, in Allen's Astrophysical Quantities, Arthur Cox editor, 2000). Ground-based white light images made from 1882 to 1976 by the Greenwich Observatory, and most recently by the U.S. Air Force operational Solar Observation Optical Network (SOON) sites. The observations of the sunspot regions are available from the National Geophysical Data Center (NGDC) operated by NOAA, at http://www.ngdc.noaa.gov/stp/SOLAR/ftpsunspotregions.html and supply the basic time-dependent information about sunspot areas and locations. Greenwich sunspot areas are re-

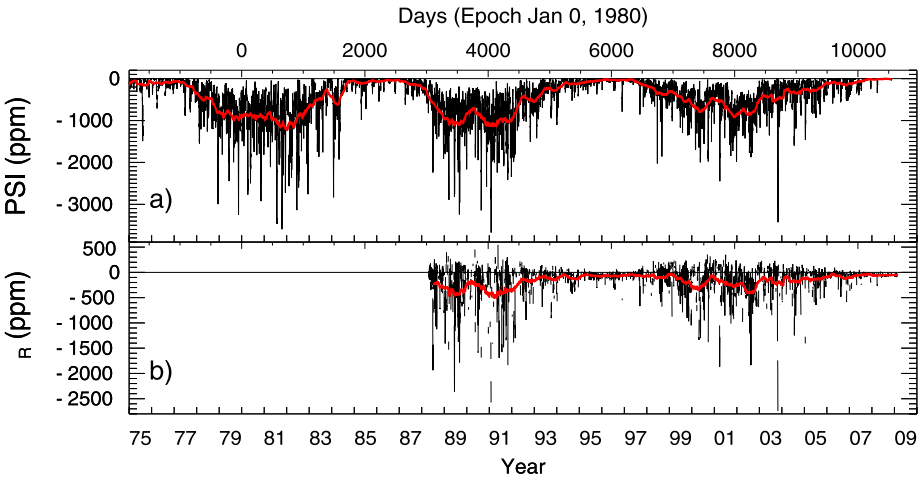

Fig. 10 Daily values of PSI calculated from Eq. 1 (**a**) and Σ_R (**b**) from the San Fernando Observatory

ported to be about 20 to 40% larger than SOON sunspot areas (Fligge and Solanki 1997; Balmaceda et al. 2005). The time series shown in Fig. 10a, is the energy reduction in total radiative output caused by sunspot darkening, P_S, calculated from SOON sunspot data archived at NOAA NGDC. There is also a different way to account for sunspots and partly faculae, that is Σ_R of the San Fernando Observatory (Preminger et al. 2002) which is shown in Fig. 10b. It provides the photometric sum of the images observed with a 10 nm-bandpass filter centered at 672.3 nm and measures the relative change in the red continuum irradiance caused by both bright and dark solar features in active regions. For comparison see also the green curve of the bottom panel of Fig. 11.

The explicit calculation of a facular index, P_F, analogous to P_S is also possible (Lean et al. 1998) but more difficult because faculae have lower contrasts in the visible spectrum and are more fragmented than sunspots. In solar images made in the core of Ca II and other strong Fraunhofer lines the emission is preferentially enhanced in chromospheric plage and bright network that overlie photospheric faculae. Ca II K images therefore provide information about facular areas and locations from which to construct facular brightening indices (Lean et al. 1998; Harvey and White 1998). Σ_K of the San Fernando Observatory, which is deduced in a similar way as Σ_R but from observations of the Ca II K emission with a 1 nm-bandpass filter at 393.4 nm was successfully used to model TSI during cycle 22 (Preminger et al. 2002), but it fails for cycle 23. Thus de Toma et al. (2004) used instead Mg II index for the facular and network contribution. Faculae and network can also be identified in magnetograms (e.g. Krivova et al. 2003, and Sect. 5.3).

The empirical models discussed here utilise as inputs indices for sunspot darkening P_S and for facular and network brightening P_F, combined in different proportions for total versus spectral irradiance at different wavelengths. Models of contemporary total and UV spectral irradiance variability, for which adequate observational databases exist, are developed in one of two ways. Either the P_F and P_S time series are regressed together against the observed irradiance, S or $F(\lambda)$, or the observations are first corrected for sunspot effects then the residual time series, $S - P_S$ or $F(\lambda) - P_S(\lambda)$, is linearly regressed against P_F (Lean et al. 1997; Fröhlich and Lean 1998a; Lean 2000). Both approaches yield an expression of the form $S(t) \propto a P_S(t) + b P_F(t)$ for total solar irradiance or $F(\lambda, t) \propto a_\lambda P_S(t) + b_\lambda P_F(t)$ for spectral irradiance at time t and wavelength λ. Thus, in empirical irradiance variability

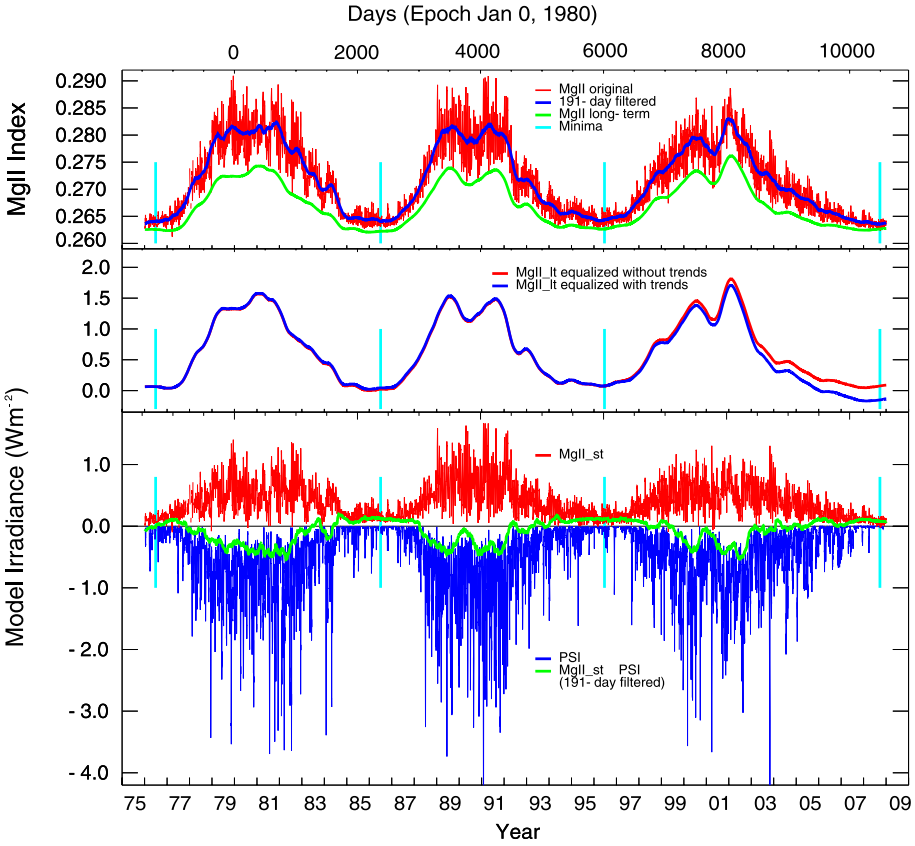

Fig. 11 *The top panel* shows the composite Mg-II index (*red*) and the long-term part, P_{Fl} determined as a lower envelope of short-term variation, P_{Fs} mainly due to the passage of faculae in active regions. *The lower two panels* show the calibrated indices: $b_{\mathrm{Fl}} P_{\mathrm{Fl}}$ (long-term Mg-II) and $b_{\mathrm{Fs}} P_{\mathrm{Fs}}$ (short-term Mg-II) together with $b_{\mathrm{S}} P_{\mathrm{S}}(t)$ (PSI). *The vertical lines* indicate the time of the solar cycle minima used to separate the cycles. *The green line in the bottom panel* shows the 191-day filtered sum of the facular and spot influence

models the indices $P_{\mathrm{S}}(t)$ and $P_{\mathrm{F}}(t)$ contain time dependent information about the sources of the irradiance variability and the (time-independent) coefficients a_λ and b_λ adjust the relative contributions of these sources for radiation at different wavelengths, or for total irradiance. In practice, the observations may or may not be detrended prior to the regression, depending on the confidence (or lack of) in their long-term stability (e.g. Lean et al. 1997).

As an example we show the results of a three-component model of Fröhlich (2009b) with sunspot darkening, P_{S}, and short and long-term facular brightening, P_{Fs} and P_{Fl}. As shown on the top panel of Fig. 11 the long-term component P_{Fl} is determined as a smoothed lower envelope of P_{F} and the short-term P_{Fs} as $P_{\mathrm{F}} - P_{\mathrm{Fl}}$. This approach better accommodates possible differences in the short and long-term sources of irradiance variability, that is the changes related to the active-region passage or to the solar-cycle modulation. As the recent minimum of TSI is lower than the ones before and the Mg II index does not show a similar change, a linear trend between each minimum has been added to the model, as a time-varying 'quiet' Sun $a(t) = a_0 + a_1 t$. Moreover, each cycle is fitted separately to allow for

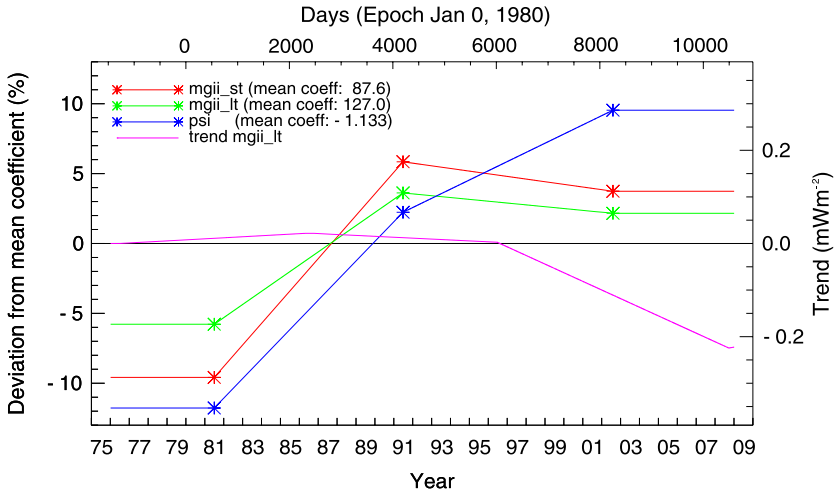

Fig. 12 Shown are the changes of the coefficients determined for each cycle relative to there mean value. These changes are then used to 'correct' the long and short-term Mg II and PSI for further analysis. Also shown are the trends needed to be introduced to account for the changes in TSI not represented by the Mg II index, nor PSI

Table 2 Coefficients according to Eq. 2 for each cycle

Parameter	Cycle 21	Cycle 22	Cycle 23	Mean	Unit
a_0	1365.45	1365.39	1365.38	1365.41	$\mathrm{W\,m^{-2}}$
a_1	0.0508	0.0056	−0.3864	–	$\mu\mathrm{W\,m^{-2}/day}$
b_{Fs}	79.20	92.71	90.87	87.6	$\mathrm{W\,m^{-2}}$/Mg-II
b_{Fl}	119.6	131.6	129.7	127.0	$\mathrm{W\,m^{-2}}$/Mg-II
b_{S}	−0.999	−1.158	−1.241	−1.133	factor

possible changes from cycle to cycle and the following relation is used

$$S(t) = a(t) + b_{\mathrm{Fs}} P_{\mathrm{Fs}}(t) + b_{\mathrm{Fl}} P_{\mathrm{Fl}}(t) + b_{\mathrm{S}} P_{\mathrm{S}}(t). \quad (2)$$

The coefficients do vary from cycle to cycle as summarised in Table 2 and Fig. 12. As the trend is part of the fitting, it may not only indicate a difference between the trends of TSI and the model, but also an intra-cycle change of some $b_{\mathrm{Fs,\,Fl\,S}}$. In general such a change indicates a change of contrast and/or area: in the case of b_{S} it is the sunspot contrast only, whereas a change in $b_{\mathrm{Fl,Fs}}$ could also be due to a change of the specific contrast of the Mg II index, that is a combination of contrast and area. It is interesting to note that all b are increasing with time and most importantly b_{S}. Also the $b_{\mathrm{Fs,\,Fl}}$ are similar for cycle 22 and 23, but nearly 15% lower during cycle 21. These differences indicate changes in the physical sources that produce the irradiance variations and further study of these differences is needed to understand the physical mechanisms, as e.g. differences in the relationship between the chromospheric brightening sampled by the Mg II index and photospheric brightening influencing TSI.

The trend during cycle 23 is mainly determined by the important trend in TSI, which will however not be discussed here as stated in Sect. 1. Moreover, the difference between b_{Fs} and b_{Fl} is interesting and shows that the contrast depends on the scale of the magnetic features—the smaller they get, the brighter they are (Spruit and Zwaan 1981). Direct observations from

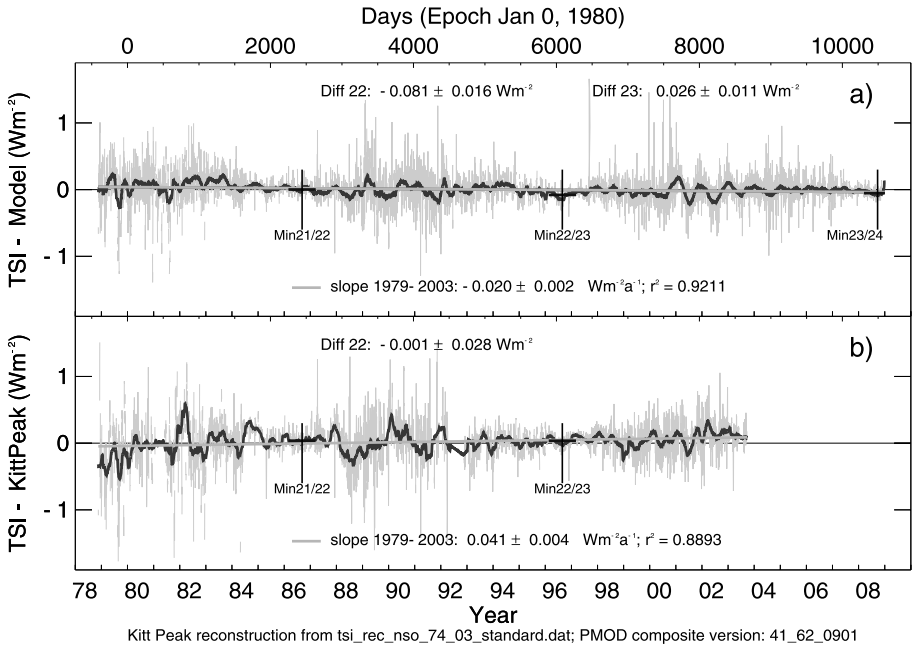

Fig. 13 Comparison of the PMOD composite (**a**) with a three-component proxy model fitted to each cycle separately as described here and in Fröhlich (2009b) and (**b**) with the reconstruction from Kitt-Peak images by Wenzler et al. (2006), and Sect. 5.3

MDI/SOHO confirm this as a function of the magnitude of the magnetic field (Ortiz et al. 2002; Ortiz 2005), which also represents the size of the features. Hence, the solar-cycle (long-term) variation seem to be dominated by the small magnetic features of the network outside the activity belts, whereas the short-term variation are due to faculae, active network and sunspots in active regions. The overall result of the model is shown in Fig. 13 together with the reconstruction from Kitt-Peak images and magnetograms discussed in Sect. 5.3. The very high correlation of $r^2 = 0.92$ is mainly achieved by fits to each cycle which was indicated by the existence of a substantial trend in TSI during cycle 23 and then provides also information about possible inter-cycle changes of the contrasts of the different features. On Fig. 13 also the Kitt-Peak reconstruction is also shown which reaches $r^2 = 0.89$ with only one adjustable parameter (see Sect. 5.3), but shows more short-term noise and also some differences between cycles 21 and 22.

The final result of 3-component proxy model are shown in Fig. 11, which shows the influence due to the variability on cycle and active-region time scales in the middle and lower panel, respectively. The 191-day filtered sum of the active region influence, the sum of the spot and facular influence (green curve in Fig. 11), indicates that the short-term variation is anti-correlated with the cycle and slightly positive over a roughly four-year period centered around the minima. This behaviour is similar to the directly observed Σ_R in Fig. 10b.

5.2 Irradiance Reconstruction from Intensity Images

The success of proxy methods in accounting for measured changes in irradiance variations on time-scales of days to years provides strong support for the hypothesis that irradiance

variations are caused by changes in the amount and distribution of magnetic flux upon the solar surface. However, methods based on employing indices provide only indirect determinations of the contribution of magnetic features in generating irradiance variations. On the other hand, methods based on spatially resolved measurements of magnetic region properties (contrast, flux) allow quantitative determinations of the contributions due to different features. These methods also allow one to study the role of possible non-magnetic mechanisms. In the following, we shall describe in greater detail the set of methods belonging to the second type. In particular, we refer to the methods proposed by Penza et al. (2003) and Fontenla and Harder (2005), henceforth called Rome and SRPM respectively.

These methods assume that the solar irradiance is given by the sum of the fluxes emerging from the different components of the solar atmosphere. At present, Rome assumes four atmosphere components (quiet Sun, facular regions, umbra, penumbra), whereas SRPM takes seven components into account (cell interior, network, active network, faint plage, bright plage, umbra, penumbra). These components are represented by the set of semi-empirical time-independent atmosphere models as described in Sect. 4. The models are used to compute the brightness spectrum of the components at a given wavelength, through spectral synthesis codes (see Sect. 4). The bolometric flux emerging from a given component is thus obtained by integrating the spectral fluxes computed over the whole range of synthesised wavelengths. Rome and SRPM reproduce irradiance variations by combining the time-independent output of these model computations with the time dependent information about the fraction of the solar disk covered by each modelled component. This latter information is obtained from the analysis of full-disk photometric observations provided by the Precision Solar Photometric Telescopes (PSPT) at the Rome and M. Loa Observatories (Coulter and Kuhn 1994; Ermolli et al. 2003; White et al. 2000). In particular, both methods make use of photospheric observations taken in the red continuum around 607 nm in order to identify dark magnetic regions, and of chromospheric observations at the Ca II K line at 393 nm in order to discern features corresponding to bright magnetic regions. Although both methods are based on similar data, the criteria applied for the identification of the atmosphere components differ in several aspects.

Rome utilises iterative procedures based on intensity thresholds and skeletonising algorithms to identify the atmospheric components. The algorithms are applied to contrast images, which are computed for each analysed observation. Notice that the several parameters used by these algorithms have been fixed independently by the output of atmospheric model computations (see, e.g., Ermolli et al. 2007). For example, contrast threshold values used for identification of umbra and penumbra regions are taken from recent high-resolution measurements published in the literature (see, e.g., Penza et al. 2006).

On the other hand, the SRPM image analysis method is mostly based on the output of Fontenla et al. (1999) and Fontenla et al. (2006) semi-empirical atmospheric computations. In particular, the criteria applied for the image decomposition represent the closest agreement between the intensity measured at each pixel and the one computed with the set of modelled atmospheres at the disk position corresponding to that of the analysed pixel.

We start with examples of Rome applications. Figure 14, adapted from Giorgi et al. (2005), shows a reconstruction of TSI variations which covers Solar Cycle 23, from July 1996 to December 2004. In this example, the daily TSI variations provided by the VIRGO team (version 5-006-0305) were compared to the daily reconstructed TSI variations, obtained as described by Penza et al. (2003) by using Rome PSPT observations. This reconstruction assumes four components (quiet Sun, umbra, penumbra and facular regions) and uses the output of the PSPT image processing described above, together with the output of the modelled atmospheres summarised in Sec. 4. In particular, it uses model C and model

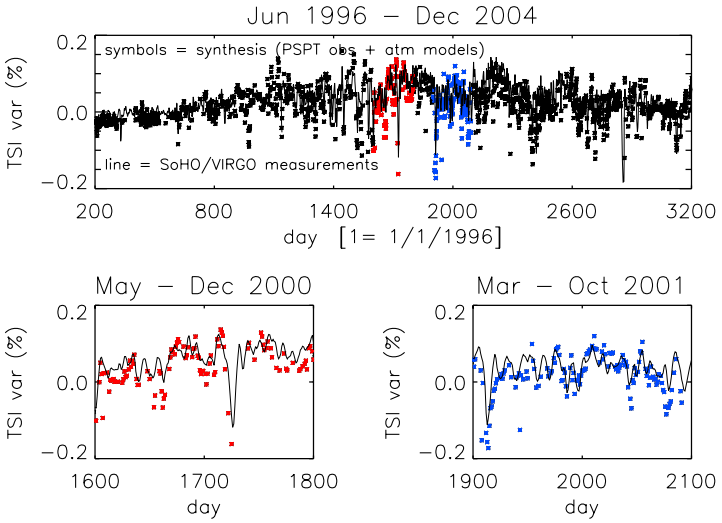

Fig. 14 Comparison between daily variations of the TSI measured by SoHO VIRGO (*line*) and those obtained with the Rome method (*symbols*) (from Giorgi et al. 2005). *Top*: 2555 daily values measured by VIRGO from July 1996 to December 2004 compared with the model. *Bottom*: details of the comparison for two short periods near the activity maximum

P computations, described in Fontenla et al. (2006) (see Table 1), for quiet Sun and facular regions, respectively. Moreover, it uses two models obtained by weighting model C computations with umbra and penumbra contrasts as measured by Tritschler and Schmidt (2002) in order to represent umbra and penumbra regions, respectively. The bolometric fluxes evaluated for the four components were then weighted with the results of the identification of components for each day of the period analysed, i.e. with the fraction of solar disk covered by each modelled component. Figure 14 also shows details of this comparison for two short periods near the activity maximum. The correlation coefficient between the measured and reconstructed variations is 0.98 for the period from 1998 to 2004.

It is worth noting that this reconstruction is obtained by assuming a fixed number of components and a fixed set of model atmospheres. The number of components used, the details of the image decomposition applied and some parameters of the model atmospheres (mainly the effective temperature of umbra and penumbra) are all important ingredients of the model and can be varied to some extent in order to improve the quality of the agreement with observed irradiance variations.

Penza et al. (2006) extended this reconstruction back to the beginning of Solar Cycle 22. In this application, the TSI composite (version 5-007-0310a) provided by the VIRGO team for the period 1978–2004 was used, together with the output of model computations quoted above, the measurements of active regions (AR) disk coverages obtained at the S. Fernando Observatory (Walton et al. 2003a, 2003b) for the period 1986–2004, and with the estimates of AR disk coverages obtained from Mg II core-to-wing index measurements for the period 1978–1985. This reconstruction also assumes four components, although these differ from the components used in the reconstruction described above. In this case, quiet Sun, network, facular and spot regions, with no distinction between umbrae and penumbrae, are now considered. Outputs of model C, model E and model F computations (Penza et al. 2004) were used to evaluate the bolometric fluxes of the quiet Sun, network and facular regions,

respectively. Model C weighted by a mean value of the contrast measurements obtained by Tritschler and Schmidt (2002) was used to describe spot regions. Finally, some functional relations among network, facular, umbra, penumbra measured disk coverages and Mg II index values are also used for the completion of the data required for the irradiance reconstruction over the whole period analysed (details are given by Penza et al. 2006).

In this reconstruction, TSI variations on the solar rotation scale are well reproduced in the period where direct measurements of AR properties are available. In contrast, only the average of TSI variations is reproduced for the period in which AR disk coverage estimates are obtained from the Mg II index proxy (cf. Fligge et al. 1998). Penza et al. (2006) also applied the same approach for the study of the cyclic modulation of the three photospheric lines (Fe I 537.9, C I 538.0 and Ti II 538.1 nm). The modelled line changes turned out to be different from the observational results obtained by Gray and Livingston (1997a, 1997b) and Livingston and Wallace (2003), either in amplitude or in phase. Penza et al. (2006) attribute this result to the larger sensitivity of modelled line characteristics to several parameters used for the atmospheric modelling (for example gravity, abundance, microturbulence), than the modelling of TSI and SSI variations.

Solar spectral irradiance modelled with SRPM compared to those measured by SIM/SORCE are presented in Fig. 15 taken from Harder et al. (2005a). This comparison covers five wavelengths in the visible and infrared and the period from October 2004 to June 2005. The measured and modelled time series show a better agreement in the range between 656 nm and 857 nm than obtained by Fontenla et al. (2004), but the model tends to underestimate the variability at shorter wavelengths. This better agreement is mainly due to the updates of facular and plage models, P and H, respectively, presented by Fontenla et al. (2006), and also due to the inclusion of a penumbra model, R, into irradiance calculations.

All the examples listed above show the general good agreement between measurements of irradiance variations and modelling obtained through the two methods considered here. Nevertheless, these figures also show that current modelling requires further investigation at some specific wavelengths. In particular, spectral syntheses have to be improved at both shorter and longer wavelengths. It is worth noting that the quality of the comparisons described is always limited by intrinsic uncertainties associated with the use of ground-based observations. These observations are not as homogeneous as those recorded from space, for example by SoHO/MDI, like those used for the modelling described in Sect. 5.3. In fact, both variable seeing and scattered light changes may significantly affect the results of the image processing for the identification of the atmosphere components, and may thus worsen the agreement between measured and reconstructed irradiance variations.

However, photometric observations like those used by Rome and SRPM were regularly recorded in several observatories since the beginning of the 20th century. These earlier observations may thus provide a further extension of the irradiance modelling with these methods to earlier cycles, which in turn may allow us insight to be gained into long-term variability mechanisms.

5.3 Irradiance Reconstruction from Magnetic Measurements

5.3.1 Total Solar Irradiance

The set of models described here uses magnetograms to identify the location of bright and dark magnetic features. The main assumption of such models is that all variations on time scales longer than approximately half a day are caused by the evolving surface distribution

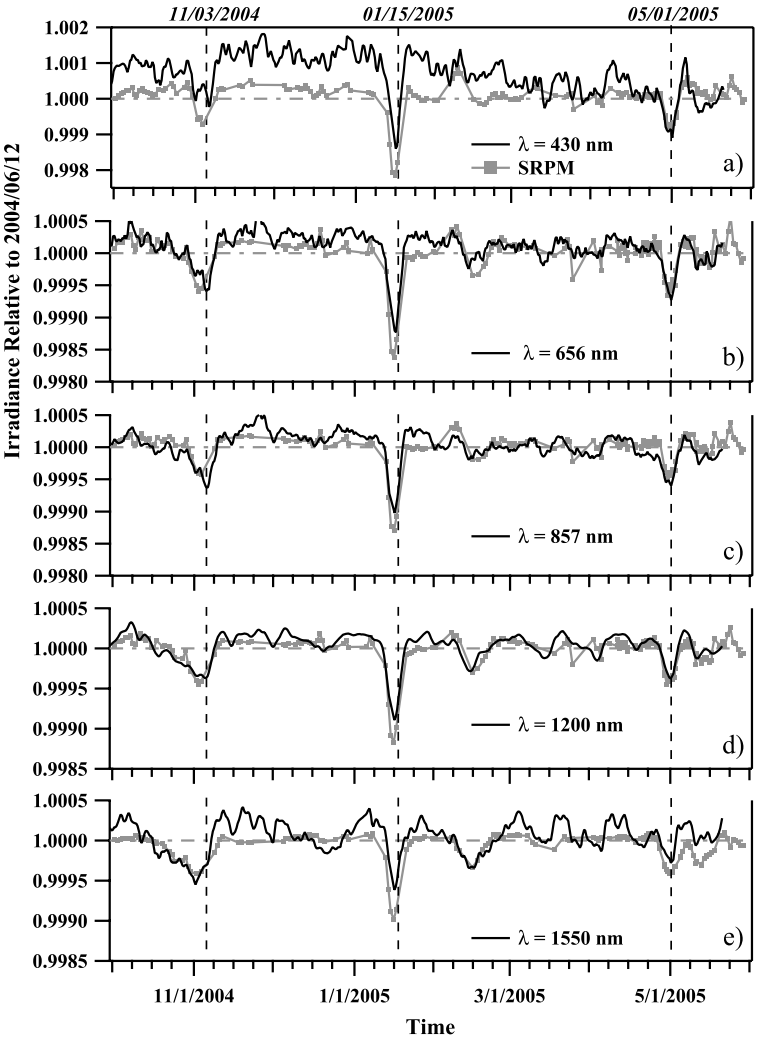

Fig. 15 Comparison of relative SIM/SORCE spectral irradiance measurements with the SRPM calculations at the same wavelengths. *The dashed vertical lines* correspond to times of sunspot passages (from Harder et al. Harder et al. 2005a)

of the Sun's magnetic field. They thus test the physical models that contend that irradiance variations are caused by the magnetic field near the solar surface (see Sect. 4). Here we describe the so-called SATIRE models (Spectral And Total Irradiance REconstructions, Solanki and Krivova 2004; Solanki et al. 2005; Krivova and Solanki 2005) which are based on this assumption and which have been worked out in greatest detail as well as having been applied most widely. As for all models described in Sect. 4, the surface magnetic features are divided into classes (atmospheric components), each described by a characteristic brightness spectrum. These spectra are calculated from the corresponding model atmospheres (Unruh et al. 1999) (see Sect. 4). In the current version of SATIRE, the solar photosphere is repre-

sented by a 4-component model. The atmospheric components and the corresponding fluxes are described in Sect. 4 (see also Table 1).

Temporal variations of the irradiance come from the second ingredient of SATIRE, the filling factors, which describe the fraction of the visible solar surface occupied by each photospheric component and evolve with time (see below for how filling factors are assigned to each magnetogram pixel). They are taken from observed magnetograms. The reconstructions made with SATIRE so far use magnetograms and continuum images recorded at the Kitt Peak National Solar Observatory (KP/NSO, Livingston et al. 1976; Jones et al. 1992) and by the Michelson Doppler Imager (MDI, Scherrer et al. 1995) on SoHO.

Intensity images are employed to identify sunspots. Different brightness thresholds are used to separate umbrae (u) and penumbrae (p). Since sunspot umbrae and penumbrae are both larger than the size of an individual pixel of either MDI or the Kitt Peak magnetographs ($2'' \times 2''$ or smaller), a pixel which falls within a sunspot umbra or penumbra is assumed to be covered by it completely. In other words, the sunspot filling factor, $\alpha_{\mathrm{u,p}}$, of such a pixel is 1. Alternatively, $\alpha_{\mathrm{u,p}} = 0$, if a pixel lies outside the sunspot.

All pixels identified as belonging to sunspots are excluded from the subsequent analysis of the magnetograms and all remaining magnetic signal above the noise level is assigned to faculae and the network, which are described by a single model atmosphere in the current version of SATIRE. Facular and network elements are typically smaller than the MDI pixel size (e.g. Solanki 1993, and Sect. 4), so that the pixel may partly also cover the quiet solar surface. To describe this state of affairs a facular filling factor, α_{f}, is introduced, which denotes the fraction of the pixel covered by the facular or network component. The filling factor, α_{f}, grows linearly with the strength of the magnetic field until the saturation magnetic flux, Φ_{sat}, at which α_{f} reaches unity. Above this flux the pixel is assumed to be completely covered by faculae ($\alpha_{\mathrm{f}} = 1$).[1] Based only on the employed magnetograms, this saturation flux cannot be fixed precisely and is thus a free parameter of the model. It is fixed from a comparison with the observed total irradiance. The physical background for this saturation lies in the different brightness of magnetic flux tubes in regions with large and small magnetic filling factors (Solanki and Stenflo 1984; Solanki 1986), which in turn is due to different average horizontal areas of individual magnetic features in such regions (Grossmann-Doerth et al. 1994). It is a crude way of describing that the bolometric, angle-integrated brightness of a solar surface element only increases up to a pixel-averaged field strength of 200–300 G, beyond which it starts to decay again (left panel of Fig. 5).

In this way, every individual pixel of a magnetogram is analysed, in order to find whether it lies within a sunspot or a facular region. Everything that does not belong to active regions and the network is counted to the quiet Sun:

$$\alpha_{\mathrm{q}} = 1 - \alpha_{\mathrm{u}} - \alpha_{\mathrm{p}} - \alpha_{\mathrm{f}} \tag{3}$$

The brightness (intensity times surface area) of each pixel, $I_{\mathrm{px}}(\mu, \lambda, t)$, is then given by

$$I_{\mathrm{px}}(\mu, \lambda, t) = \sum_{i=\mathrm{q,u,p,f}} \alpha_{\mathrm{i,px}}(t) I_{\mathrm{i}}(\mu; \lambda), \tag{4}$$

[1] $\alpha_{\mathrm{f}} = 1$ does not mean that the pixel is completely covered by field, only that the modified model P of Fontenla et al. (1999) is used to describe that pixel in unadulterated form. It is currently unknown to what magnetic flux densities or filling factors the various Fontenla et al. (1999, 2006) atmospheric models correspond to.

where $\mu = \cos\theta$ and θ is the heliocentric angle, λ is the wavelength, t time and $I_{q,u,p,f}$ are the intensities of the quiet Sun, umbrae, penumbrae and faculae (including the network), respectively. The sum over all pixels gives the solar irradiance at a given wavelength and an integral over all wavelengths the total solar irradiance. More details on the SATIRE models are provided by Fligge et al. (2000).

Different reconstructions have been carried out using the SATIRE model. Initially the most homogeneous available data set, the one from MDI, was used to reconstruct solar irradiance during cycle 23. It was important to use 5-minute averaged magnetograms, since the noise level in the standard 1-minute magnetograms is too high to provide accurate results. With a single free parameter both the short-(days to weeks) and long-term (years to the solar cycle) variations of the total irradiance could be reproduced. The correlation coefficient between the measured (VIRGO) and modelled irradiances is 0.96 (Krivova et al. 2003) for the period 1996–2002.

Employing KP/NSO data allowed an extension of the reconstruction back to 1974, i.e. to the time before the first satellite measurements of solar irradiance. These data suffer from variable seeing and artifacts in some of the images (Wenzler et al. 2004, 2005, 2006). More seriously, the data were not recorded by the same instrument over the whole period. The first, the 512-channel Diode Array Magnetograph (Livingston et al. 1976), was improved a few times and was, in 1992, replaced by the spectromagnetograph (Jones et al. 1992). Unfortunately, the earlier data remain of a noticeably lower quality. For example, it is impossible to distinguish between umbrae and penumbrae in older images and only the entire spot areas can be determined. Therefore the average ratio of umbral to sunspot area was determined for the period after 1992 and assumed to be the same over the earlier period (Wenzler et al. 2006). As expected, the resulting reconstructed irradiance reproduces the TSI measurements (PMOD composite; see Fig. 16) somewhat less well than the MDI-based model. But, again, the agreement is quite good on both short and long time scales. The correlation coefficient is 0.91 for the whole period (1978–2003), 0.94 for the period after 1992 and no bias has been found between the three activity cycles (Wenzler et al. 2006). This means that the evolution of the solar surface magnetic field indeed explains most irradiance variations during the period considered.

One possible improvement for the future is to use products of numerical simulations, rather than empirical model atmospheres. In such an approach one could employ the output of realistic 3-D numerical simulations of magnetoconvection, such as those described by Vögler et al. (2005), see Sect. 3.2 to compute the emergent spectrum. First calculations for the disc centre have been done by Unruh et al. (2009) but they need to be extended to cover the whole solar disc. Instead of magnetograms, it is also possible to use flux transport simulations, such as those of Schrijver et al. (2003), or Baumann et al. (2004, 2006). This is of particular interest for extending the simulations further back in time when no magnetograms were available. However, in both cases, the model will have to be adapted (e.g. to the lower spatial resolution of the magnetic field mas produced by flux transport simulations).

5.3.2 Spectral Solar Irradiance

A major advantage of reconstructions based on model atmospheres, such as SATIRE is that they provide both the total and spectral irradiance. Here we briefly consider how SATIRE compares with different observations.

Longwards of 400 nm, the model can be tested against VIRGO measurements in three spectral channels, red, green and blue centred at 862, 500 and 402 nm, respectively. The agreement on time scales of up to a few months is very good (Krivova et al. 2003) but on

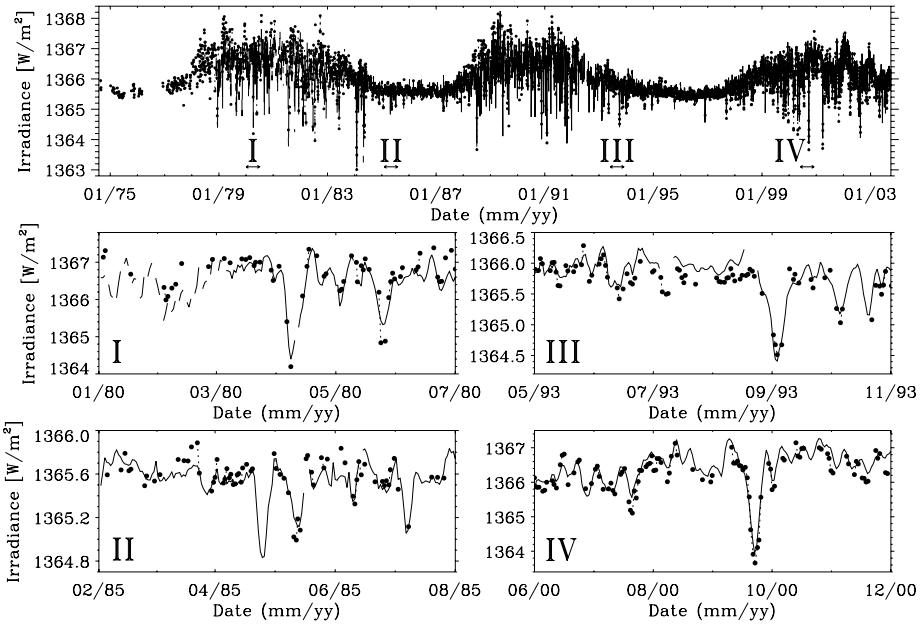

Fig. 16 *Top panel*: The reconstructed TSI (*filled circles*, connected by *dotted curve* when there are no data gaps) based on NSO/KP data between 1974 and 2003. *The solid line* represents the measured total solar irradiance (PMOD composite, Fröhlich 2005) between 1978 and 2003. *The bottom panels* are enlargements of four shorter intervals at different activity levels from different cycles (from Wenzler et al. 2006)

longer time scales the trends in the data introduced by the degradation of the sensitivity of the VIRGO Sun-photometers remains a problem for such a comparison. Note that the free parameter, $\Phi_{\rm sat}$, is set from a comparison of the model with TSI and is kept the same when considering the spectral irradiance.

Unruh et al. (2008) have also compared the calculated irradiance with SORCE/SIM measurements in the range between 200 and 1600 nm over a time span of three solar rotations in 2004. In most wavelength regions, the variability agrees well between the observations and the model calculations. The model does particularly well between 400 and 1300 nm, but fails below 220 nm (cf. Fig. 17), as well as for some of the strong NUV lines. Due to the low sensitivity of SORCE for wavelengths between approximately 310 and 350 nm, the model calculations still provide the best estimates of solar variability in this range.

The modelled spectra can also be compared with spectra recorded by, e.g., the SUSIM instrument on UARS (Brueckner et al. 1993). Figure 17 shows the spectrum measured on a particular day by SUSIM (solid curve) and as obtained from the model (dashed). Above 300 nm the model is in good agreement with the measurements. Although stronger lines are not perfectly reproduced in the range between 200 and 300 nm, on average the model gives reasonable results here as well. At shorter wavelengths, the LTE approximation involved in calculations of the model atmospheres fails and the model spectrum lies systematically too low. Using a non-LTE approximation is one obvious, although tedious, line of attack on the problem (e.g. Fontenla et al. 1999, 2006; Haberreiter et al. 2005, 2008a).

Krivova et al. (2006) have developed an alternative technique allowing an empirical extension of the SATIRE models down to 115 nm with the help of SUSIM data. As Fig. 18 shows, the model by Krivova et al. (2003) reproduces irradiance variations in the range

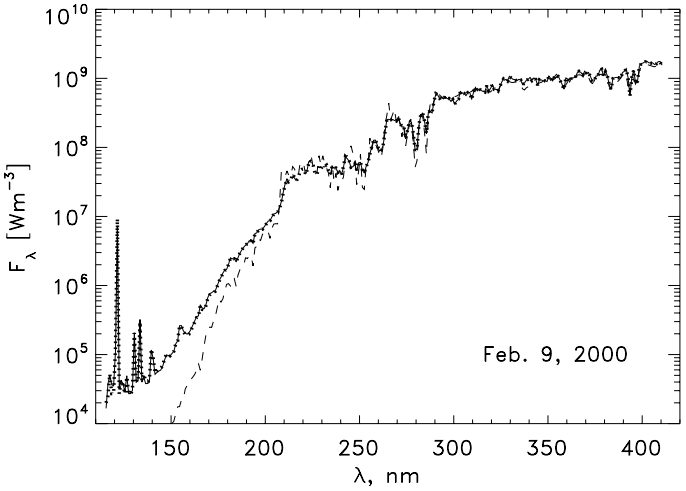

Fig. 17 Solar UV spectrum on December 11, 2000: observed (*solid curve*) by SUSIM on UARS (Brueckner et al. 1993; Floyd et al. 2003) and modelled (*dashed*) following Krivova et al. (2003). *The dotted line* shows the empirical model by Krivova et al. (2006)

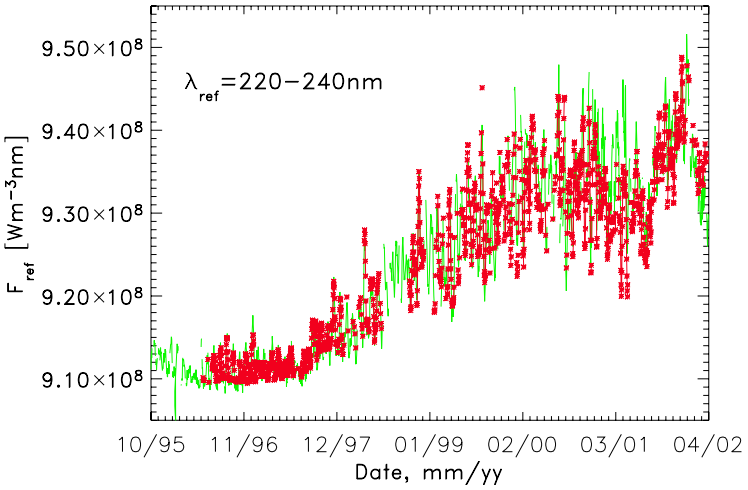

Fig. 18 The solar irradiance integrated over the wavelength range 220–240 nm as a function of time during 1996–2002. *The solid line* represents SUSIM measurements and *asterisks* the model by Krivova et al. (2003). The correlation coefficient between the model and the data is $r_c = 0.97$ ($r_c^2 = 0.94$)

220–240 nm relatively well. On the other hand, SUSIM measurements can be used in order to work out empirical relations between the irradiance in this wavelength range and the irradiance at every other wavelength at which the data exist, i.e. between 115 and 410 nm. Krivova et al. (2006) employ daily level 3BS V21 data with spectral sampling of 1 nm (Floyd et al. 2003). The deduced relations are then used to calculate irradiance at every wavelength within this range (dotted line in Fig. 17) from the reconstructed irradiance at 220–240 nm. Figure 19 shows the calculated solar Ly-α irradiance (Krivova and Solanki 2008) compared

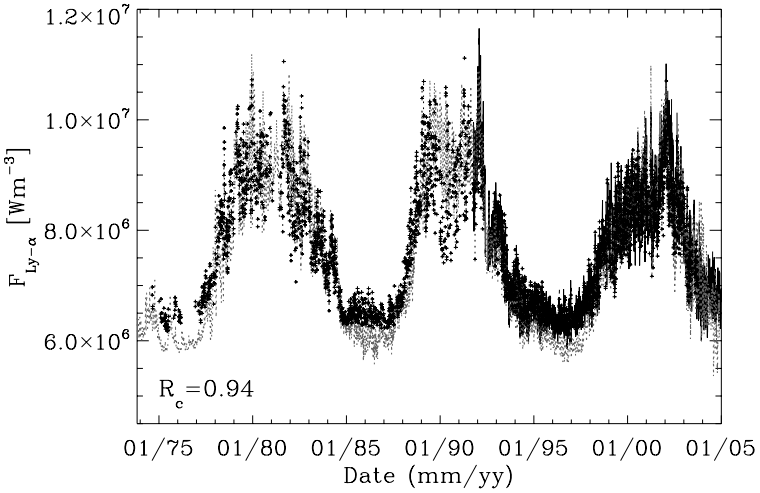

Fig. 19 Solar Ly-α irradiance since 1974: reconstructed (+), measured by SUSIM (*solid line*; Floyd et al. 2003) and compiled by Woods et al. (2000) (*dotted line*). The correlation coefficient between the model and the composite is 0.94. From Krivova and Solanki (2008)

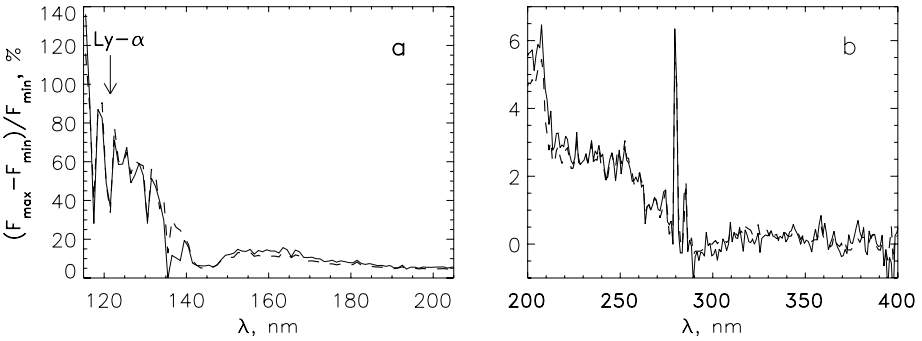

Fig. 20 Relative irradiance variations between the solar spectrum at activity maximum (2-month average, April–May 2000) and minimum (2-month average, October–November, 1996) at (**a**) 115–210 nm and (**b**) 200–420 nm. *The solid line* represents SUSIM measurements and *the dashed line* the model by Krivova et al. (2006)

to SUSIM measurements and to the composite of UARS SOLSTICE measurements and related proxy models by Woods et al. (2000). Note that the latter record is adjusted to the UARS SOLSTICE absolute values, so that the difference between the two models is only due to the difference of about 5% in the magnitude of the Ly-α cycle shown by SUSIM and SOLSTICE. Other than that, the model agrees well with the completely independent composite time series, with a correlation coefficient of 0.94.

Figure 20 displays the relative irradiance variations between activity maximum (2 month average over April–May 2000) and minimum (October–November 1996). The solid line represents SUSIM measurements and the dashed line the reconstruction by Krivova et al. (2006). The figure demonstrates the consistency between the empirical extension of the SATIRE model and the SUSIM measurements.

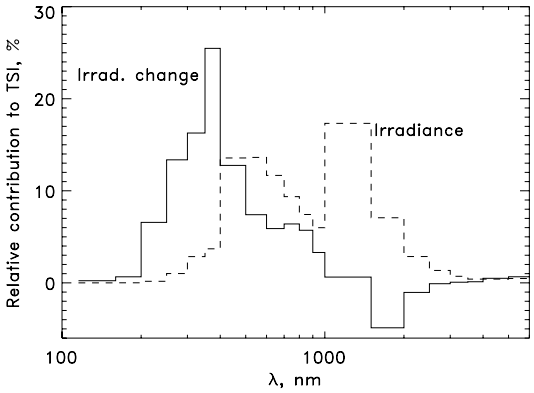

Fig. 21 The histograms of the spectral distribution of the solar irradiance (*dashed*) and of the solar cycle irradiance variations (*solid*; from Krivova et al. 2006). Note different size of bins (50 nm at $\lambda \leq 400$ nm, 100 nm at 400 nm $< \lambda \leq 1000$ nm and 2000 nm at longer λ)

The calculated contribution of different wavelength ranges to solar irradiance and its 11-year cycle variation is shown in Fig. 21. The dashed line describes the distribution of the energy (irradiance) over the solar spectrum. Note the different size of bins: 50 nm in the UV, 100 nm in the visual and 2000 nm in the IR. The solid line shows the spectral distribution of the irradiance changes over the solar cycle. Although about 30% of solar energy comes from the long wavelengths (>1000 nm), their contribution to the TSI variations is small: according to the model/SATIRE it is negative at 1000–3000 nm due to sunspots and is about 1–1.5% at yet longer λ. In contrast, the contribution of the UV to TSI variations is very high: the wavelength interval 300–400 nm accounts for about 40% of the TSI variations and about 60% of all TSI variations originate in the range between 200 nm and 400 nm. Recent estimates based on SCIAMACHY measurements gave a value of 55% for the contribution of the 200–400 nm spectral range to the irradiance variations in cycle 23 (Pagaran et al. 2009). Of course, it will be particularly interesting to test the spectral irradiance due to the SATIRE models using the SORCE (Harder et al. 2005b) and SCIAMACHY (Skupin et al. 2005) spectral irradiance measurements on time scales longer than a solar rotation.

5.3.3 Spectral Solar Irradiance from NLTE Calculations

Haberreiter et al. (2005) combined the filling factors derived from the MDI and KP magnetograms and continuum images by Krivova et al. (2003) and Wenzler et al. (2004, 2005) with radiances for the quiet Sun, sunspots and faculae calculated with their NLTE code COSI, in order to calculate irradiance variations in the UV. Figure 22 shows the reconstruction for Lyman α compared with the composite by Woods et al. (2000). The comparison shows that the variability of the reconstructed Lyman α is considerably lower than observations suggest. The reasons for this discrepancy can be attributed to the following points.

Firstly, the population numbers of hydrogen are strongly influenced by the ambipolar diffusion, a process by which protons (and hydrogen atoms) diffuse from higher to lower (lower to higher) layers in the solar atmosphere. The protons recombine at the lower layers and thereby lead to an increase of the hydrogen population. Consequently, the Lyman α flux is increased (Fig. 8; for details see Fontenla et al. 1993). This process has not been accounted for in the reconstruction shown in Fig. 22.

Secondly, the fact that the UV is formed higher up in the solar atmosphere, but the feature identification from magnetograms represents photospheric layers, also needs to be included in the reconstruction. As the magnetic field expands with increasing height in the solar atmosphere, an increase in the area covered by the active region has to be accounted for. One

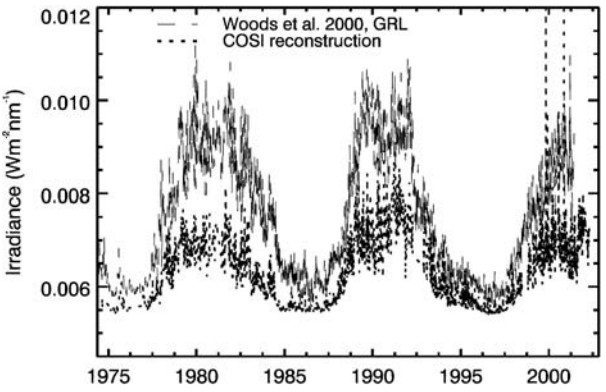

Fig. 22 Reconstruction of Lyman α based on radiance calculations with the COSI code and the Fontenla et al. (1999) atmosphere structures. The reconstruction is compared with the Lyman α composite by Woods et al. (2000); Adopted from Haberreiter et al. (2005)

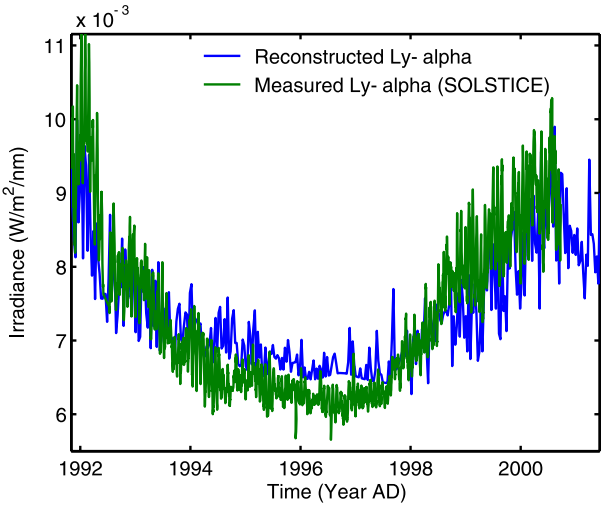

Fig. 23 Comparison of the reconstructed Lyman α irradiance compared with SOLSTICE measurements (Schöll and Schmutz 2008)

way to achieve this is to use additional chromospheric observations for the feature identification and relate them to a height dependence of area covered by active regions. Schöll and Schmutz (2008) introduced the so-called active area expansion (AAE) parameter to account for this effect. They determined the AAE parameter from a comparison of photospheric images and observations taken with the SOHO/SUMER instrument in Lyman ε. This comparison leads to an AAE factor of the order of 2.5. Figure 23 shows the Lyman α reconstruction taking into account the AAE parameter (blue line), leading to an improved agreement of the reconstruction with the SOLSTICE observations (green line).

6 Discussion and Conclusion

Models of the solar total irradiance have progressed to the stage where it is possible to reproduce the directly observed variations with high accuracy (Sect. 5). This suggests that a good understanding of the mechanisms of these variations has been reached. One such set of models, the SATIRE models, uses intensity spectra of the Sun's different photospheric magnetic components calculated from the corresponding model atmospheres and information (from

models or observations) on the distribution of the magnetic flux on the solar surface, in order to figure out the total and spectral irradiance variations. The model works well for the total irradiance and in the spectral ranges longwards of about 200–300 nm where it has been tested. A recently developed empirical technique based on the observed SUSIM spectra allows an empirical extension of the SATIRE models to shorter wavelengths (down to about 115 nm), which are of great interest to Sun-climate studies. Reconstructions of solar UV irradiance based on NLTE spectral synthesis of radiance spectra have also being progressing. Besides, first encouraging tests of the models have been carried out in the IR (Fontenla et al. 2006; Platnick and Fontenla 2008; Unruh et al. 2008). More work is still needed in these directions. Magnetohydrodynamic model simulations of photospheric magnetoconvection also support the idea that surface magnetism is the main source of short term, i.e. shorter than a solar cycle, irradiance variations.

These models can account for most of the variance in the observed irradiance time series. This shows that additional contributions to the TSI variation from photospheric temperature variations outside spots and magnetic brightening must be small, although the low TSI value during the most recent minimum may point to still another mechanism for changes on century time scales. As photometric observations like those used today by the Rome and SRPM models were regularly recorded at several observatories since the beginning of the 20th century (Ermolli et al. 2009; Foukal et al. 2009) they may provide a further extension of the irradiance modelling with these methods to earlier cycles, which in turn may allow insight to be gained into long term variability mechanisms as indicated by recent TSI observations.

Acknowledgements Most of this work has been performed within the framework of an ISSI Research Team during the period of 2004–2006. The continuous support by ISSI (International Space Science Institute, Bern, Switzerland) is gratefully acknowledged. A part of this work was supported by DFG (Deutsche Forschungsgemeinschaft) grant No. SO 711/1-2 and by the WCU (Science and Engineering Foundation) grant No. R31-10016 from the Korean Ministry of Education, Science and Technology

References

V.I. Abramenko, D.W. Longcope, Distribution of the magnetic flux in elements of the magnetic field in active regions. Astrophys. J. **619**, 1160–1166 (2005)

H.M. Antia, Does the Sun shrink with increasing magnetic activity? Astrophys. J. **590**, 567–572 (2003)

E.H. Avrett, R. Loeser, Models of the solar chromosphere and transition region from SUMER and HRTS observations: Formation of the extreme-ultraviolet spectrum of Hydrogen, Carbon, and Oxygen. Astrophys. J. Suppl. Ser. **175**, 229–276 (2008). doi:10.1086/523671

S.M. Bailey, T.N. Woods, C.A. Barth, S.C. Solomon, L.R. Canfield, R. Korde, Measurements of the solar soft X-ray irradiance by the Student Nitric Oxide Explorer: First analysis and underflight calibrations. J. Geophys. Res. **105**, 27179–27194 (2000)

L. Balmaceda, S.K. Solanki, N. Krivova, A cross-calibrated sunspot areas time series since 1874. Mem. Soc. Astron. Ital. **76**, 929–932 (2005)

I. Baumann, D. Schmitt, M. Schüssler, S.K. Solanki, Evolution of the large-scale magnetic field on the solar surface: A parameter study. Astron. Astrophys. **426**, 1075–1091 (2004)

I. Baumann, D. Schmitt, M. Schüssler, A necessary extension of the surface flux transport model. Astron. Astrophys. **446**, 307–314 (2006)

D.J. Bercik, A. Nordlund, R.F. Stein, Magnetoconvection and micropores, in *Local and Global Helioseismology: The Present and Future*, ed. by H. Sawaya-Lacoste (European Space Agency, ESA SP-517, 2003), pp. 201–206

G.E. Brueckner, K.L. Edlow, L.E. Floyd, J.L. Lean, M.E. Vanhoosier, The solar ultraviolet spectral irradiance monitor (SUSIM) experiment on board the Upper Atmosphere Research Satellite (UARS). J. Geophys. Res. **98**(17), 10695–10711 (1993)

K.A. Burlov-Vasiljev, Y.B. Matvejev, I.E. Vasiljeva, Results of the solar disk-center spectral intensity measurements in the range 310–1070 nm, in *Solar Analogs: Characteristics and Optimum Candidates*, ed. by J.C. Hall. Second Annual Lowell Observatory Fall Workshop (1998), pp. 115–122

R. Cameron, A. Vögler, M. Schüssler, V. Zakharov, Simulations of solar pores, in *The Dynamic Sun: Challenges for Theory and Observations*, ed. by D. Danesy, S. Poedts, A. De Groof, J. Andries (European Space Agency, ESA SP-600, 2005), p. 11.1

M. Carlsson, R.F. Stein, Å. Nordlund, G.B. Scharmer, Observational manifestations of solar magnetoconvection: Center-to-limb variation. Astrophys. J. Lett. **610**, L137–L140 (2004)

G.A. Chapman, On the energy balance of solar active regions. Nature **308**, 252–254 (1984)

G.A. Chapman, A.M. Cookson, J.J. Dobias, Variations in total solar irradiance during solar cycle 22. J. Geophys. Res. **101**, 13541–13548 (1996)

W.H. Chiang, P.V. Foukal, The influence of faculae on sunspot heat blocking. Sol. Phys. **97**, 9–20 (1985)

R.L. Coulter, J.R. Kuhn, RISE/PSPT as an Experiment to Study Active Region Irradiance and Luminosity Evolution, in *Solar Active Region Evolution: Comparing Models with Observations*, ed. by K.S. Balasubramaniam, G.W. Simon. Proceedings of the Fourteenth (14th) International Summer Workshop, National Solar Observatory Sacramento Peak, Sunspot, New Mexico, USA, 30 August – 3 September 1993, Astronomical Society of the Pacific Conference Series, vol. 68 (1994)

B. De Pontieu, M. Carlsson, R. Stein, L. Rouppe van der Voort, M. Löfdahl, M. van Noort, Å. Nordlund, G. Scharmer, Rapid temporal variability of faculae: High-resolution observations and modeling. Astrophys. J. **646**, 1405–1420 (2006)

G. de Toma, O.R. White, G.A. Chapman, S.R. Walton, D.G. Preminger, A.M. Cookson, Solar cycle 23: An anomalous cycle? Astrophys. J. **609**, 1140–1152 (2004)

W. Deinzer, G. Hensler, M. Schüssler, E. Weisshaar, Model calculations of magnetic flux tubes. I—Equations and method. II—Stationary results for solar magnetic elements. Astron. Astrophys. **139**, 426–449 (1984). URL http://adsabs.harvard.edu/cgi-bin/nph-bib_query?bibcode=1984A%26A...139..426D&db_key=AST

S. Dewitte, D. Crommelinck, S. Mekaoui, A. Joukoff, Measurement and uncertainty of the long-term total solar irradiance trend. Sol. Phys. **224**, 209–216 (2004)

G.R.R.F. Donnelly, F. Cowley, Solar X-Ray Measurements From SMS-1, SMS-2, and GOES-1: Information for data users, NOAA Technical Memorandum ERL SEL-48 (1977)

A. Egidi, B. Caccin, S. Sofia, W. Heaps, W. Hoegy, L. Twigg, High-precision measurements of the solar diameter and oblateness by the Solar Disk Sextant (SDS) experiment. Sol. Phys. **235**, 407–418 (2006)

I. Ermolli, F. Berrilli, A. Florio, A measure of the network radiative properties over the solar activity cycle. Astron. Astrophys. **412**, 857–864 (2003)

I. Ermolli, S. Criscuoli, M. Centrone, F. Giorgi, V. Penza, Photometric properties of facular features over the activity cycle. Astron. Astrophys. **465**, 305–314 (2007)

I. Ermolli, S.K. Solanki, A.G. Tlatov, N.A. Krivova, R.K. Ulrich, J. Singh, Comparison among Ca II K spectroheliogram time series with an application to solar activity studies. Astrophys. J. **698**, 1000–1009 (2009)

M. Fligge, S.K. Solanki, Inter–cycle variations of solar irradiance: Sunspot areas as a pointer. Sol. Phys. **173**, 427–439 (1997)

M. Fligge, S.K. Solanki, Y.C. Unruh, C. Fröhlich, C. Wehrli, A model of solar total and spectral irradiance variations. Astron. Astrophys. **335**, 709–718 (1998)

M. Fligge, S.K. Solanki, Y.C. Unruh, Modelling irradiance variations from the surface distribution of the solar magnetic field. Astron. Astrophys. **353**, 380–388 (2000)

L.E. Floyd, J.W. Cook, L.C. Herring, P.C. Crane, SUSIM'S 11-year observational record of the solar UV irradiance. Adv. Sp. Res. **31**, 2111–2120 (2003)

J. Fontenla, G. Harder, Physical modeling of spectral irradiance variations. Mem. Soc. Astron. Ital. **76**, 826–833 (2005)

J. Fontenla, O.R. White, P.A. Fox, E.H. Avrett, R.L. Kurucz, Calculation of solar irradiances. I. Synthesis of the solar spectrum. Astrophys. J. **518**, 480–499 (1999)

J.M. Fontenla, E.H. Avrett, R. Loeser, Energy balance in the solar transition region. I—hydrostatic thermal models with ambipolar diffusion. Astrophys. J. **355**, 700–718 (1990)

J.M. Fontenla, E.H. Avrett, R. Loeser, Energy balance in the solar transition region. II—effects of pressure and energy input on hydrostatic models. Astrophys. J. **377**, 712–725 (1991)

J.M. Fontenla, E.H. Avrett, R. Loeser, Energy balance in the solar transition region. III—Helium emission in hydrostatic, constant-abundance models with diffusion. Astrophys. J. **406**, 319–345 (1993)

J.M. Fontenla, J. Harder, G. Rottman, T.N. Woods, G.M. Lawrence, S. Davis, The signature of solar activity in the infrared spectral irradiance. Astrophys. J. Lett. **605**, L85–L88 (2004)
J.M. Fontenla, E. Avrett, G. Thuillier, J. Harder, Semiempirical models of the solar atmosphere. I. The quiet- and active Sun photosphere at moderate resolution. Astrophys. J. **639**, 441–458 (2006)
J.M. Fontenla, K.S. Balasubramaniam, J. Harder, Semiempirical models of the solar atmosphere. II. The quiet-Sun low chromosphere at moderate resolution. Astrophys. J. **667**, 1243–1257 (2007). doi:10.1086/520319
P. Foukal, L.A. Fowler, M. Livshits, A thermal model of sunspot influence on solar luminosity. Astrophys. J. **267**, 863–871 (1983)
P. Foukal, L. Bertello, W.C. Livingston, A.A. Pevtsov, J. Singh, A.G. Tlatov, R.K. Ulrich, A Century of solar Ca ii measurements and their implication for solar UV driving of climate. Sol. Phys. **255**, 229–238 (2009). doi:10.1007/s11207-009-9330-0
P.V. Foukal, L.A. Fowler, A photometric study of heat flow at the solar photosphere. Astrophys. J. **281**, 442–454 (1984)
L.A. Fowler, P.V. Foukal, T.L. Duvall Jr., Sunspot bright rings and the thermal diffusivity of solar convection. Sol. Phys. **84**, 33–44 (1983)
C. Fröhlich, Observations of irradiance variability. Space Sci. Rev. **94**, 15–24 (2000)
C. Fröhlich, Total solar irradiance: The PMOD-composite (2005). A description of the construction and the newest version of the composite can be found at http://www.pmodwrc.ch/pmod.php?topic=tsi/composite/SolarConstant
C. Fröhlich, Solar irradiance variability since 1978. Space Sci. Rev. **125**, 53–65 (2006)
C. Fröhlich, *Solar Radiometry*, ISSI Scientific Reports, vol. 10, ESA Publication Division, Noordwijk, The Netherlands, chap 32. (2009a, in press)
C. Fröhlich, Total solar irradiance variability: What have we learned about its variability from the record of the last three solar cycles? in *Climate and Weather of the Sun-Earth System (CAWSES): Selected Papers from the 2007 Kyoto Symposium, October 23–27, 2007*, ed. by T. Tsuda, R. Fujii, K. Shibata, M. Geller (Terra Publishing, Tokyo, 2009b), pp. 217–230. URL: http://www.terrapub.co.jp/onlineproceedings/ste/CAWSES2007/index.html
C. Fröhlich, J. Lean, The sun's total irradiance: Cycles and trends in the past two decades and associated climate change uncertainties. Geophys. Res. Lett. **25**, 4377–4380 (1998a)
C. Fröhlich, J. Lean, Total solar irradiance variations: The construction of a composite and its comparison with models, in *IAU Symposium 185: New Eyes to See Inside the Sun and Stars*, ed. by F.L. Deubner, J. Christensen-Dalsgaard, D. Kurtz (Kluwer Academic, Dordrecht, 1998b), pp. 89–102
C. Fröhlich, J. Lean, Solar radiative output and its variability: Evidence and mechanisms. Astron. Astrophys. Rev. **12**, 273–320 (2004)
C. Fröhlich, D. Crommelynck, C. Wehrli, M. Anklin, S. Dewitte, A. Fichot, W. Finsterle, A. Jiménez, A. Chevalier, H.J. Roth, In-flight performances of VIRGO solar irradiance instruments on SOHO. Sol. Phys. **175**, 267–286 (1997)
F. Giorgi, I. Ermolli, M. Centrone, E. Marchei, Calibration of the Arcetri solar archive images. Mem. Soc. Astron. Ital. **76**, 977 (2005)
D.F. Gray, W.C. Livingston, Monitoring the solar temperature: Empirical calibration of the temperature sensitivity of Ci lambda 5380. Astrophys. J. **474**, 798–801 (1997a)
D.F. Gray, W.C. Livingston, Monitoring the solar temperature: Spectroscopic temperature variations of the Sun. Astrophys. J. **474**, 802–809 (1997b)
R.O. Gray, C.J. Corbally, The calibration of MK spectral classes using spectral synthesis. 1: The effective temperature calibration of dwarf stars. Astron. J. **107**, 742–746 (1994)
U. Grossmann-Doerth, M. Knoelker, M. Schuessler, S.K. Solanki, The deep layers of solar magnetic elements. Astron. Astrophys. **285**, 648–654 (1994)
M. Haberreiter, I. Hubeny, E. Rozanov, I. Rüedi, W. Schmutz, T. Wenzler, Towards a spherical code for the evaluation of solar UV-bands that influence the chemical composition in the stratosphere, in *Proceedings of the SOHO 11 Symposium on From Solar Min to Max: Half a Solar Cycle with SOHO*, ed. by A. Wilson. ESA SP, vol. 508 (ESA Publications Division, Noordwijk, 2002), p. 209
M. Haberreiter, N.A. Krivova, W. Schmutz, T. Wenzler, Reconstruction of the solar UV irradiance back to 1974. Adv. Space Res. **35**, 365–369 (2005)
M. Haberreiter, W. Schmutz, I. Hubeny, NLTE model calculations for the solar atmosphere with an iterative treatment of opacity distribution functions. Astron. Astrophys. **492**, 833 (2008a). 0810.3471
M. Haberreiter, W. Schmutz, A.G. Kosovichev, Solving the discrepancy between the seismic and photospheric solar radius. Astrophys. J. Lett. **675**, L53–L56 (2008b). doi:10.1086/529492, 0711.2392
J. Harder, J. Fontenla, O. White, G. Rottman, T. Woods, Solar spectral irradiance variability comparisons of the SORCE SIM instrument with monitors of solar activity and spectral synthesis. Mem. Soc. Astron. Ital. **76**, 735–742 (2005a)

J. Harder, G. Lawrence, J. Fontenla, G. Rottman, T. Woods, The spectral irradiance monitor: Scientific requirements, instrument design, and operation modes. Sol. Phys. **230**, 141–167 (2005b)
K.L. Harvey, O.R. White, Spectral irradiances and magnetic structures. Astron. Soc. Pacific Conf. Ser. **140**, 247–252 (1998)
D.F. Heath, B.M. Schlesinger, The Mg-280 nm doublet as a monitor of changes in solar ultraviolet irradiance. J. Geophys. Res. **91**, 8672–8682 (1986)
D.V. Hoyt, H.L. Kyle, J.R. Hickey, R.H. Maschhoff, The NIMBUS-7 solar total irradiance: A new algorithm for its derivation. J. Geophys. Res. **97**, 51–63 (1992)
H.S. Hudson, Observed variability of the solar luminosity. Annu. Rev. Astron. Astrophys. **26**, 473–507 (1988)
H.S. Hudson, R.C. Willson, SMM experiment: Initial observations by the active cavity radiometer. Adv. Space Res. **1**(13), 285–288 (1981)
H.S. Hudson, S. Silva, M. Woodard, R.C. Willson, The effects of sunspots on solar irradiance. Sol. Phys. **76**, 211–218 (1982)
H.P. Jones, T.L. Duvall, J.W. Harvey, C.T. Mahaffey, J.D. Schwitters, J.E. Simmons, The NASA/NSO spectromagnetograph. Sol. Phys. **139**, 211–232 (1992)
C.U. Keller, M. Schüssler, A. Vögler, V. Zakharov, On the origin of solar faculae. Astrophys. J. **607**, L59–L62 (2004)
O. Kjeldseth-Moe, P. Maltby, A model for the penumbra of sunspots. Sol. Phys. **8**, 275 (1969)
G. Kopp, G. Lawrence, The Total Irradiance Monitor (TIM): Instrument design. Sol. Phys. **230**, 91–109 (2005)
N.A. Krivova, S.K. Solanki, Modelling of irradiance variations through atmosphere models. Mem. Soc. Astron. Ital. **76**, 834–841 (2005)
N.A. Krivova, S.K. Solanki, Models of solar irradiance variations: Current status. J. Astrophys. Astron. **29**, 151–158 (2008). doi:10.1007/s12036-008-0018-x
N.A. Krivova, S.K. Solanki, M. Fligge, Y.C. Unruh, Reconstruction of solar irradiance variations in cycle 23: Is solar surface magnetism the cause? Astron. Astrophys. **399**, L1–L4 (2003)
N.A. Krivova, S.K. Solanki, L. Floyd, Reconstruction of solar UV irradiance in cycle 23. Astron. Astrophys. **452**, 631–639 (2006)
N.A. Krivova, L. Balmaceda, S.K. Solanki, Reconstruction of solar total irradiance since 1700 from the surface magnetic flux. Astron. Astrophys. **467**, 335–346 (2007). doi:10.1051/0004-6361:20066725
J.R. Kuhn, R.I. Bush, M. Emilio, P.H. Scherrer, On the constancy of the solar diameter. II. Astrophys. J. **613**, 1241–1252 (2004)
R. Kurucz, New opacity calculations, in *Stellar Atmospheres: Beyond Classical Models*, ed. by L. Crivellari, I. Hubeny, D. Hummer. NATO ASI Ser. C, vol. 341 (Kluwer Academic, Dordrecht, 1991), pp. 441–448
R. Kurucz, The solar spectrum, in *Solar Interior and Atmosphere*, ed. by A. Cox, W. Livingston, M. Matthews (University of Arizona Press, Tucson, 1991), pp. 663–669
R. Kurucz, *ATLAS9 Stellar Atmosphere Programs and 2 km/s Grid*. ATLAS9 Stellar Atmosphere Programs and 2 km/s Grid Kurucz CD-ROM No. 13 (Cambridge: Smithsonian Astrophysical Observatory, 1993)
J. Lean, Evolution of the Sun's spectral irradiance since the maunder minimum. Geophys. Res. Lett. **27**, 2425–2428 (2000)
J.L. Lean, G.J. Rottman, H.L. Kyle, T.N. Woods, J.R. Hickey, L.C. Puga, Detection and parameterization of variations in solar mid and near ultraviolet radiation (200 to 400 nm). J. Geophys. Res. **102**, 29939–29946 (1997)
J.L. Lean, J. Cook, W. Marquette, A. Johannesson, Magnetic sources of the solar irradiance cycle. Astrophys. J. **492**, 390–401 (1998)
R.B. Lee III, B.R. Barkstrom, R.D. Cess, Characteristics of the earth radiation budget experiment solar monitors. Appl. Opt. **26**, 3090–3096 (1987)
R.B. Lee III, M.A. Gibson, R.S. Wilson, S. Thomas, Long-term total solar irradiance variability during sunspot cycle 22. J. Geophys. Res. **100**, 1667–1675 (1995)
P. Lemaire, P. Gouttebroze, J.C. Vial, G.E. Artzner, Physical properties of the solar chromosphere deduced from optically thick lines. I—Observations, data reduction, and modelling of an average plage. Astron. Astrophys. **103**, 160–176 (1981)
B.W. Lites, G.B. Scharmer, T.E. Berger, A.M. Title, Three-dimensional structure of the active region photosphere as revealed by high angular resolution. Sol. Phys. **221**, 65–84 (2004)
W. Livingston, L. Wallace, The Sun's immutable basal quiet atmosphere. Sol. Phys. **212**, 227–237 (2003)
W. Livingston, J. Harvey, O. Malanushenko, L. Webster, Sunspot Magnetic Fields Measured up to 6000 Gauss, in *Solar Active Regions and 3D Magnetic Structure*. 26th Meeting of the IAU, Joint Discussion 3, 16–17 August, 2006, Prague, Czech Republic, JD03, #54 3 (2006)
W.C. Livingston, J. Harvey, C. Slaughter, D. Trumbo, Solar magnetograph employing integrated diode arrays. Appl. Opt. **15**, 40–52 (1976)

P. Maltby, E.H. Avrett, M. Carlsson, O. Kjeldseth-Moe, R.L. Kurucz, R. Loeser, A new sunspot umbral model and its variation with the solar cycle. Astrophys. J. **306**, 284–303 (1986)
S.K. Mathew, V. Martínez Pillet, S.K. Solanki, N.A. Krivova, Properties of sunspots in cycle 23. I. Dependence of brightness on sunspot size and cycle phase. Astron. Astrophys. **465**, 291–304 (2007). arXiv:astro-ph/0701401
R.G.W.E. McClintock, T. Woods, Solar-Stellar Irradiance Comparison Experiment II (SOLSTICE II): Instrument concept and design. Sol. Phys. **230**, 225–258 (2005)
N. Meunier, Statistical properties of magnetic structures: Their dependence on scale and solar activity. Astron. Astrophys. **405**, 1107–1120 (2003)
H. Neckel, D. Labs, The solar irradiance between 3300 and 12500å. Sol. Phys. **90**, 205–258 (1984)
F. Noël, On solar radius variations observed with astrolabes. Sol. Phys. **232**, 127–141 (2005)
A. Nordlund, H.C. Spruit, H.G. Ludwig, R. Trampedach, Is stellar granulation turbulence? Astron. Astrophys. **328**, 229–234 (1997)
A. Ortiz, Solar cycle evolution of the contrast of small photospheric magnetic elements. Adv. Space Res. **35**, 350–360 (2005)
A. Ortiz, S.K. Solanki, V. Domingo, M. Fligge, B. Sanahuja, On the intensity contrast of solar photospheric faculae and network elements. Astron. Astrophys. **388**, 1036–1047 (2002)
J.A. Pagaran, M. Weber, J.P. Burrows, Solar variability from 240 to 1750 nm in terms of faculae brightening and sunspot darkening from SCIAMACHY. Astrophys. J. (2009, in press)
V. Penza, B. Caccin, I. Ermolli, M. Centrone, M.T. Gomez, Modeling solar irradiance variations through PSPT images and semiempirical models, in *ESA SP-535: Solar Variability as an Input to the Earth's Environment*, ed. by A. Wilson (2003), pp. 299–302
V. Penza, B. Caccin, I. Ermolli, M. Centrone, Comparison of model calculations and photometric observations of bright "magnetic" regions. Astron. Astrophys. **413**, 1115–1123 (2004)
V. Penza, E. Pietropaolo, W. Livingston, Modeling the cyclic modulation of photospheric lines. Astron. Astrophys. **454**, 349–358 (2006)
S. Platnick, J.M. Fontenla, Model calculations of solar spectral irradiance in the 3.7-μm band for Earth remote sensing applications. J. Appl. Meteorol. Climatol. **47**, 124 (2008). doi:10.1175/2007JAMC1571.1
D.G. Preminger, S.R. Walton, G.A. Chapman, Photometric quantities for solar irradiance modeling. J. Geophys. Res. (Space Phys.) **107**, 1354 (2002) (6.1–6.6)
M.P. Rast, P.A. Fox, H. Lin, B. Lites, R.W. Meisner, O.R. White, Bright rings around sunspots. Nature **401**, 678–680 (1999)
C.S. Rosenthal, J. Christensen-Dalsgaard, Å. Nordlund, R.F. Stein, R. Trampedach, Convective contributions to the frequencies of solar oscillations. Astron. Astrophys. **351**, 689–700 (1999)
N. Scafetta, R.C. Willson, ACRIM-gap and TSI trend issue resolved using a surface magnetic flux TSI proxy model. Geophys. Res. Lett. **36**, 5701 (2009). doi:10.1029/2008GL036307
P.H. Scherrer, R.S. Bogart, R.I. Bush, J.T. Hoeksema, A.G. Kosovichev, J. Schou, W. Rosenberg, L. Springer, T.D. Tarbell, A. Title, C.J. Wolfson, I. Zayer, MDI Engineering Team, The solar oscillations investigation—Michelson Doppler imager. Sol. Phys. **162**, 129–188 (1995)
G. Schmidtke, R. Brunner, D. Eberhard, B. Halford, U. Klocke, M. Knothe, W. Konz, W.J. Riedel, H. Wolf, SOL ACES: Auto-calibrating EUV/UV spectrometers for measurements onboard the international space station. Adv. Space Res. **37**, 273–282 (2006a). doi:10.1016/j.asr.2005.01.112
G. Schmidtke, C. Fröhlich, G. Thuillier, ISS-SOLAR: Total (TSI) and spectral (SSI) irradiance measurements. Adv. Space Res. **37**, 255–264 (2006b). doi:10.1016/j.asr.2005.01.009
M. Schöll, W. Schmutz, Reconstructing the spectral solar irradiance: The active area expansion. PMOD/WRC Annual Report 2007 p. 28 (2008)
C.J. Schrijver, M.L. DeRosa, A.M. Title, Asterospheric magnetic fields and winds of cool stars. Astrophys. J. **590**, 493–501 (2003)
M. Schüssler, A. Vögler, Magnetoconvection in a sunspot umbra. Astrophys. J. Lett. **641**, L73–L76 (2006). astro-ph/0603078
M. Schüssler, S. Shelyag, S. Berdyugina, A. Vögler, S.K. Solanki, Why solar magnetic flux concentrations are bright in molecular bands. Astrophys. J. **597**, L173–L176 (2003)
S. Shelyag, M. Schüssler, S.K. Solanki, S.V. Berdyugina, A. Vögler, G-band spectral synthesis and diagnostics of simulated solar magneto-convection. Astron. Astrophys. **427**, 335–343 (2004)
J. Skupin, S. Noël, M.W. Wuttke, M. Gottwald, H. Bovensmann, M. Weber, J.P. Burrows, SCIAMACHY solar irradiance observation in the spectral range from 240 to 2380 nm. Adv. Space Res. **35**, 370–375 (2005)
S. Sofia, Global variability of the Sun. Mem. Soc. Astron. Ital. **69**, 531–537 (1998)
S. Sofia, Variations of total solar irradiance produced by structural changes of the solar interior. EOS Trans. **85**, 217–221 (2004)
S.K. Solanki, Velocities in solar magnetic fluxtubes. Astron. Astrophys. **168**, 311–329 (1986)

S.K. Solanki, Small-scale solar magnetic fields: An overview. Space Sci. Rev. **63**, 1–188 (1993)
S.K. Solanki, Sunspots: An overview. Astron. Astrophys. Rev. **11**, 153–286 (2003). doi:10.1007/s00159-003-0018-4
S.K. Solanki, N.A. Krivova, Solar irradiance variations: From current measurements to long-term estimates. Sol. Phys. **224**, 197–208 (2004)
S.K. Solanki, J.O. Stenflo, Properties of solar magnetic fluxtubes as revealed by Fe I lines. Astron. Astrophys. **140**, 185–198 (1984)
S.K. Solanki, A.D. Seleznyov, N.A. Krivova, Solar irradiance fluctuations on short timescales. ESA SP **535**, 285–588 (2003)
S.K. Solanki, N.A. Krivova, T. Wenzler, Irradiance models. Adv. Space Res. **35**, 376–383 (2005)
S.K. Solanki, B. Inhester, M. Schüssler, The solar magnetic field. Rep. Prog. Phys. **69**, 563–668 (2006)
H. Spruit, Theory of luminosity and radius variations, in *Sun in Time*, ed. by C. Sonnet, M.S. Giampapa, M.S. Matthews (University of Arizona Press, Tucson, 1991), pp. 118–158
H.C. Spruit, Pressure equilibrium and energy balance of small photospheric fluxtubes. Sol. Phys. **50**, 269–295 (1976)
H.C. Spruit, Heat flow near obstacles in the solar convection zone. Sol. Phys. **55**, 3–34 (1977)
H.C. Spruit, The flow of heat near a starspot. Astron. Astrophys. **108**, 356–360 (1982)
H.C. Spruit, C. Zwaan, The size dependence of contrasts and numbers of small magnetic flux tubes in an active region. Sol. Phys. **70**, 207–228 (1981). doi:10.1007/BF00151329
R.F. Stein, Å. Nordlund, Solar small-scale magnetoconvection. Astrophys. J. **642**, 1246–1255 (2006)
O. Steiner, Radiative properties of magnetic elements. II. Center to limb variation of the appearance of photospheric faculae. Astron. Astrophys. **430**, 691–700 (2005)
K.F. Tapping, B. Detracey, The origin of the 10.7 cm flux. Sol. Phys. **127**, 321–332 (1990)
G. Thuillier, M. Hersé, D. Labs, T. Foujols, W. Peetermans, D. Gillotay, P.C. Simon, H. Mandel, The solar spectral irradiance from 200 to 2400 nm as measured by the SOLSPEC spectrometer from the atlas and Eureca missions. Sol. Phys. **214**, 1–22 (2003). doi:10.1023/A:1024048429145
A. Tritschler, W. Schmidt, Sunspot photometry with phase diversity. II. Fine-structure characteristics. Astron. Astrophys. **388**, 1048–1061 (2002)
Y.C. Unruh, S.K. Solanki, M. Fligge, The spectral dependence of facular contrast and solar irradiance variations. Astron. Astrophys. **345**, 635–642 (1999)
Y.C. Unruh, N.A. Krivova, S.K. Solanki, J.W. Harder, G. Kopp, Spectral irradiance variations: comparison between observations and the SATIRE model on solar rotation time scales. Astron. Astrophys. **486**, 311–323 (2008). doi:10.1051/0004-6361:20078421, 0802.4178
Y.C. Unruh, S.K. Solanki, M. Schüssler, A. Vögler, D. Garcia-Alvarez, Towards long-term solar irradiance modelling: Network contrasts from magneto-convection simulations, in *Proceedings of the 15th Cambridge Workshop on Cool Stars, Stellar Systems and the Sun*. AIP Conference Proceedings, vol. 1094 (2009), pp. 768–771
J.E. Vernazza, E.H. Avrett, R. Loeser, Structure of the solar chromosphere. III—Models of the EUV brightness components of the quiet-sun. Astrophys. J. Suppl. Ser. **45**, 635–725 (1981)
R.A. Viereck, L.E. Floyd, P.C. Crane, T.N. Woods, B.G. Knapp, G. Rottman, M. Weber, L.C. Puga, M.T. DeLand, A composite Mg II index spanning from 1978 to 2003. Space Weather **2**, S10005 (2004)
A. Vögler, Three-dimensional simulations of magneto–convection in the solar photosphere, PhD thesis, University of Göttingen, Germany (2003). http://webdoc.sub.gwdg.de/diss/2004/voegler
A. Vögler, On the effect of photospheric magnetic fields on solar surface brightness: Results of radiative MHD simulations. Mem. Soc. Astron. Ital. **76**, 842–849 (2005)
A. Vögler, S. Shelyag, M. Schüssler, F. Cattaneo, T. Emonet, T. Linde, Simulations of magneto-convection in the solar photosphere. Equations, methods, and results of the MURaM code. Astron. Astrophys. **429**, 335–351 (2005)
S.R. Walton, D.G. Preminger, G.A. Chapman, A statistical analysis of the characteristics of sunspots and faculae. Sol. Phys. **213**, 301–317 (2003a)
S.R. Walton, D.G. Preminger, G.A. Chapman, The contribution of faculae and network to long-term changes in the total solar irradiance. Astrophys. J. **590**, 1088–1094 (2003b)
T. Wenzler, Reconstruction of Solar Irradiance Variations in Cycles 21–23 based on Surface Magnetic Fields, PhD thesis, ETH Nr 16199, Eidgenössische Technische Hochschule, Zürich (2005)
T. Wenzler, S.K. Solanki, N.A. Krivova, D.M. Fluri, Comparison between KPVT/SPM and SoHO/MDI magnetograms with an application to solar irradiance reconstructions. Astron. Astrophys. **427**, 1031–1043 (2004)
T. Wenzler, S.K. Solanki, N.A. Krivova, Can surface magnetic fields reproduce solar irradiance variations in cycles 22 and 23? Astron. Astrophys. **432**, 1057–1061 (2005)
T. Wenzler, S.K. Solanki, N.A. Krivova, C. Fröhlich, Reconstruction of solar irradiance variations in cycles 21–23 based on surface magnetic fields. Astron. Astrophys. **460**, 583–595 (2006). doi:10.1051/0004-6361:20065752

O.R. White, P.A. Fox, R. Meisner, M.P. Rast, E. Yasukawa, D. Koon, C. Rice, H. Lin, J. Kuhn, R. Coulter, Data from the precision solar photometric telescope (Pspt) in Hawaii from March 1998 to March 1999. Space Sci. Rev. **94**, 75–82 (2000)

R.C. Willson, Irradiance observations from SMM, UARS and ATLAS experiments, in *The Sun as a Variable Star, Solar and Stellar Irradiance Variations*, ed. by J. Pap, C. Fröhlich, H.S. Hudson, S. Solanki (Cambridge University Press, Cambridge, 1994), pp. 54–62

R.C. Willson, Total solar irradiance trend during solar cycles 21 and 22. Science **277**, 1963–1965 (1997), see also comment by R. Kerr on page 1923 of the same issue of Science

R.C. Willson, The ACRIMSAT/ACRIM III experiment: Extending the precision, long-term total solar irradiance climate database. Earth Obs. **13**, 14–17 (2001)

R.C. Willson, H.S. Hudson, Solar luminosity variations in solar cycle 21 **332**, 810–812 (1988)

R.C. Willson, A.V. Mordvinov, Secular total solar irradiance trend during solar cycles 21–23. Geophys. Res. Lett. **30**, 1199 (2003)

R.C. Willson, S. Gulkis, M. Janssen, H.S. Hudson, G.A. Chapman, Observations of solar irradiance variability. Science **211**, 700–702 (1981)

P.R. Wilson, Theories of sunspot structure and evolution, in *Physics of Sunspots*, ed. by L. Cram, J. Thomas (Sacramento Peak Obs, Sunspot, 1982), pp. 83–97

T.N. Woods, G.J. Rottman, *Solar Ultraviolet Variability Over Time Periods of Aeronomic Interest, Atmospheres in the Solar System: Comparative Aeronomy* (2002), p. 221

T.N. Woods, W.K. Tobiska, G.J. Rottman, J.R. Worden, Improved solar Lyman$_\alpha$ irradiance modeling from 1947 through 1999 based on UARS observations. J. Geophys. Res. **105**(A12), 27195–27216 (2000)

T.N. Woods, F.G. Eparvier, S.M. Bailey, P.C. Chamberlin, J. Lean, G.J. Rottman, S.C. Solomon, W.K. Tobiska, D.L. Woodraska, Solar EUV Experiment (SEE): Mission overview and first results. J. Geophys. Res. (Space Phys.) **110**, A01312 (2005a)

T.N. Woods et al., XUV Photometer System (XPS): Overview and calibrations. Sol. Phys. **230**, 345–374 (2005b)

T.N. Woods, G. Kopp, P.C. Chamberlin, Contributions of the solar ultraviolet irradiance to the total solar irradiance during large flares. J. Geophys. Res. (Space Phys.) **111** (2006). doi:10.1029/2005JA011507

H.J. Zahid, H.S. Hudson, C. Fröhlich, Total solar irradiance variation during rapid sunspot growth. Sol. Phys. **222**, 1–15 (2004)